



1

2

Effects of topographic and meteorological parameters

3

on the surface area loss of ice aprons in the Mont-Blanc massif (European Alps)

4

5 Suvrat Kaushik^{1,2}, Ludovic Ravanel^{1,3}, Florence Magnin¹, Yajing Yan², Emmanuel Trounev², Di-

6 ego Cusicanqui⁴

7

8 ¹ EDYTEM, Univ. Savoie Mont-Blanc, Univ. Grenoble Alpes, CNRS, 73000 Chambéry, France

9 ² LISTIC, Univ. Savoie Mont Blanc, Polytech, F-74944 Annecy-le-Vieux, France

10 ³ Department of Geosciences, University of Oslo, Sem Sælands vei 1, 0371 Oslo, Norway

11 ⁴ IGE, Univ. Grenoble Alpes - CNRS, F-38000 Grenoble, France

12 **Correspondence:** Suvrat Kaushik (suvrat.kaushik@univ-smb.fr)

13

14

15 Abstract

16 Ice aprons (IAs) are part of the critical components of the Alpine cryosphere. As a result of the
17 changing climate over the past few decades, deglaciation has resulted in a surface decrease of IAs,
18 which has not yet been documented out of a few specific examples. In this study, we quantify the
19 effects of climate change on IAs since the mid-20th century in the Mont-Blanc massif (western
20 European Alps). We then evaluate the role of climate forcing parameters and the local topography
21 in the behaviour of IAs. We precisely mapped the surface areas of 200 IAs using high-resolution
22 aerial and satellite photographs from 1952, 2001, 2012 and 2019. From the latter inventory, the
23 surface area of the present individual IAs ranges from 0.001 to 0.04 km². IAs have lost their surface
24 area over the past 70 years, with an alarming increase since the early 2000s. The total area, from
25 7.93 km² in 1952, was reduced to 5.91 km² in 2001 (-25.5 %) before collapsing to 4.21 km² in
26 2019 (-47 % since 1952). We performed a regression analysis using temperature and precipitation
27 proxies to understand better the effects of climate forcing parameters on IA surface area variations.
28 We found a strong correlation between both proxies and the relative area loss of IAs, indicating
29 the significant influence of the changing climate on the evolution of IAs. We also evaluated the



30 role of the local topographic factors in the IAs area loss. At a regional scale, factors like direct
31 solar radiation and elevation have an important influence on the behaviour of IAs, while others
32 like curvature, slope, and size of the IAs seem to be rather important on a local scale.

33

34 **Key words:** Ice aprons, surface area loss, topographic factors, meteorological parameters, Mont
35 Blanc massif.

36

37

38 **1 Introduction**

39

40 The predicted shift in climate dynamics over the next decades will undoubtedly have severe
41 consequences on the high mountain environments, primarily on glacier extent (Rafiq and Mishra,
42 2016; Kraaijenbrink et al., 2017; IPCC, 2021), permafrost (Magnin et al., 2017) and ice and snow
43 cover (Rastner et al., 2019; Guillet and Ravel, 2020). The effects of climate change on glaciers
44 constitute a remarkably well-discussed topic in the scientific community (Yalcin, 2019).

45 Climatic factors (mainly temperature and precipitation) are the main driving forces responsible for
46 these changes (Scherler et al., 2011; Bolch et al., 2012; Davies et al., 2012). Shifting temperature
47 and precipitation trends leads to the advance or retreat of glaciers both in volume and surface area
48 (Liu et al., 2013; Yang et al., 2019). On a regional and global scale, many authors have studied the
49 impacts of climate warming on glacier retreats and, consequently, on the hydrology of the
50 mountain environments (*e.g.*, Baraer et al. (2012); Sorg et al. (2014); Frans et al. (2016); Coppola
51 et al. (2018)).

52 However, as observed by Furbish and Andrews (1984), Oerlemans et al. (1998), Hoelzle et al.
53 (2003) and Salerno et al. (2017), glaciers present in the same climate regime can respond to climate
54 change in different ways. The local climate variations can partly explain these variable responses.
55 However, many of these variations result from different morphometric (size, shape, length) and
56 topographic (altitude, slope, aspect, curvature, terrain ruggedness) characteristics.

57 Several studies have been devoted to understanding the linkage between topographic factors and
58 the response of glacier/ice bodies (*e.g.*, Davies et al., 2012; De Angelis, 2014; Salerno et al., 2017).

59



60 World Glacier Monitoring Service (WGMS) monitors glacier changes in all the major mountain
61 regions of the world. However, most mapping and monitoring studies on a global scale focus on
62 massive glaciers since they are generally assessable and easier to monitor compared to other ice
63 features (Liu et al., 2013).

64 Studies are rare for small glaciers or ice bodies, which generally show a more pronounced response
65 to climate change (Oerlemans and Reichert, 2000; Triglav-Čekada and Gabrovec, 2013; Fischer
66 et al., 2015). This has led to a critical gap in our understanding of their behaviour and mass balance
67 estimates. As part of this trend, ice aprons (IAs), sometimes also referred to as ‘rock faces partially
68 covered with ice’ (Gruber and Haeberli, 2007; Hasler et al., 2011), have also received poor
69 attention from the scientific community.

70 These small ice accumulations on steep rock slopes are commonly found in all significant
71 glacierized basins worldwide. However, a concrete and well-summarised definition for IAs is still
72 missing from the literature. Previously, many authors like Benn and Evans (2010), Singh et al.
73 (2011) and Cogley et al. (2011) tried to define IAs, but the most precise definition for IAs up to
74 now can be found in Guillet and Ravanel (2020) for the Mont-Blanc massif (MBM; European
75 Alps). These authors defined IAs as "very small (typically smaller than 0.1 km² in extent) ice
76 bodies of irregular outline, lying on slopes >40°, regardless of whether they are thick enough to
77 deform under their weight". The small spatial extent of the IAs makes them very difficult to map
78 and monitor. Also, they are typically present in extremely challenging topographies on isolated
79 steep slopes. Cogley et al. (2011) specified that IAs are "lying above the head of a glacial
80 bergschrund which separates the flowing glacier ice from the stagnant ice, or a rock headwall".

81 Because of their presence on steep slopes, IAs are essential natural elements for the practice of
82 mountaineering, especially in famous destinations like MBM (Barker, 1982). IAs are passing
83 points for most classic mountaineering routes (Mourey et al., 2019). Hence, the loss of IAs is a
84 severe threat to the iconic practice of mountaineering, inscribed in 2019 by UNESCO on the
85 Representative List of the Intangible Cultural Heritage of Humanity. IAs on steep rock walls also
86 carry the critical role of covering steep rock slopes and preventing them from direct exposure to
87 direct solar radiation, thus partly preventing the warming of the underlying permafrost. In addition,
88 a recent study by Guillet et al. (2021) showed that the ice present at the base of the Triangle du
89 Tacul IA could be older than 3 ka, making IAs a potential important glacial heritage.



90 Guillet and Ravanel (2020) showed that IAs in the MBM have lost mass since the Little Ice Age
91 (LIA). Based on six different IAs, their study also showed an acceleration in the shrinkage since
92 the 1990s. They linked the loss of IA area with meteorological parameters, mainly air temperature
93 and precipitation. It was thus the first documented evidence that IAs have been losing ice volume
94 due to the changing climate. However, since this study was local and based on only a few IAs, the
95 authors could not consider other factors such as the local topography, critical for small glacier
96 bodies (Hock, 2003; Laha et al., 2017).

97 Thus, to overcome these limitations, we propose a global analysis to ascertain the relationship of
98 the area loss of IAs with the meteorological parameters, mainly air temperature and precipitation,
99 using a more comprehensive database (*c.* 200 IAs) covering the whole MBM. The large inventory
100 of IAs has been surveyed thanks to high-resolution aerial and satellite images from 1952, 2001,
101 2012 and 2019. Further, based on our inventory, we also evaluate the impacts of the
102 topographic/geometric controls on the area changes of IAs. For this, we consider the size of IA,
103 elevation/altitude, slope, curvature, Topographic Ruggedness Index (TRI), direct solar radiation
104 and permafrost conditions (classified together as topographic factors) based on past studies on
105 similar themes (*e.g.*, Oerlemans et al., 1998; Warren, 2008; DeBeer and Sharp, 2009; Jiskoot et
106 al., 2009; Davies et al., 2012; Salerno et al., 2017).

107

108

109 **2 Study area and the impacts of climate change in the region**

110

111 The Mont-Blanc massif (Fig. 1) is located in the north-western (external) Alps between France,
112 Switzerland, and Italy. It covers *c.* 550 km² and displays some of the highest peaks in the European
113 Alps; a dozen peaks have elevations greater than 4000 m a.s.l. MBM thus shows a significant
114 variation in the elevation range throughout the massif; the lowest point of the massif is at 1050 m
115 a.s.l. (Chamonix) and the highest, the top of Mont Blanc at 4808 m a.s.l.

116 Because of its high elevation, the MBM is also the most glacierized massif in the French Alps
117 (Gardent et al., 2014). There are about 100 glaciers often bordered by steep rock walls, including
118 12 glaciers larger than 5 km². The steep and irregular terrain facilitates the development of many
119 unique ice bodies like cold-based hanging glaciers or IAs. As a result of an asymmetry of the
120 massif, 6 of its largest glaciers are located on its NW French side, where slopes are gentler than



121 the Italian side and glaciers are well fed by the westerly winds while melting is reduced by the
122 protection of the shaded North faces. The SE Italian side is characterized by smaller glaciers and
123 generally steeper slopes bounded by very high sub-vertical rock walls. This asymmetry is also
124 evidenced by the difference in climatic conditions observed on the two sides of the massif. For
125 example, the Mean Annual Air Temperature (MAAT) recorded in Chamonix (at 1044 m a.s.l.) is
126 +7.2°C while that in Courmayeur (1223 m a.s.l.) is + 10.4°C (Deline et al., 2012). Comparing the
127 annual MAAT values from 1934 to today shows that MAAT increased by > 2.1°C in Chamonix
128 (*MétéoFrance* data). Moreover, the increase in MAAT from 1970 to 2009 was almost four times
129 faster than from 1934 to 1970 (Mourey et al., 2019). Not only at lower elevations, but the MAAT
130 also increased by 1.4°C at elevations exceeding 4000 m a.s.l. between 1990 and 2014 (Gilbert and
131 Vincent, 2013). The MBM has experienced nine summers characterized by heatwaves (where
132 maximum temperatures for at least three consecutive days exceed a heatwave temperature
133 threshold defined for the region) since 1990 (1994, 2003, 2006, 2009, 2015, 2017, 2018, 2019 and
134 2020), with the one as recent as 2018 being the second (after 2003) hottest. The average annual
135 precipitation recorded for Chamonix is 1,288 mm, and 854 mm for Courmayeur (Vincent, 2002).
136 The precipitation rates in the MBM have remained relatively constant since the end of the LIA,
137 but there is a noticeable decrease in the number of snowfall days relative to the total precipitation
138 days below 2700 m a.s.l. (Serquet et al., 2011).

139 Global warming has led to a general retreat trend of the MBM glaciers since the end of the LIA
140 despite small re-advances culminating in 1890, the 1920s and the 1980s (Bauder et al., 2007). The
141 recorded loss of glacier surface area was 24 % of the total area from the end of the LIA to 2008
142 (Gardent et al., 2014). The reported loss of ice thickness is also noteworthy. For example, the loss
143 of ice thickness at the front of the “Mer de Glace” glacier (1650 m a.s.l.) from 1986 to 2021 is 145
144 m; the Argentière glacier (1900 m a.s.l.) has lost 80 m in thickness from 1994 to 2013 (Bauder et
145 al., 2007). At 3550 m a.s.l., the surface of the Géant glacier also lowered by 20 m between 1992
146 and 2012 (Ravanel et al., 2013). The glacier retreat and shrinkage concur with the Equilibrium
147 Line Altitude (ELA) that rose by 170 m between 1984 and 2010 in the western Alps (Rabatel et
148 al., 2013). As a result of the loss of ice volume, the density of open crevasses has considerably
149 increased, along with an increase in bare ice areas. In some instances, loss of ice volume leads to
150 instability of steep slopes, and serac falls from the front of warm and cold glaciers are more
151 frequent (Fischer et al., 2006). This latter process can be typical during the warmest periods of the



152 year (Deline et al., 2012). Warming trends also intensify moraine erosion, leading to an increased
153 frequency of rockfalls and landslides (Deline et al., 2015; Ravelin et al., 2018).
154 Degradation/warming is another critical concern for permafrost (e.g., Haeberli and Gruber, 2009).

155

156

157 **3 Data description**

158

159 This section describes all the datasets obtained from diverse sources used in this study (Table. 1).

160

161 **3.1 Digital Elevation Model**

162

163 Since one of the main aims of our study is to perform a joint analysis of the behaviour of small ice
164 bodies and the local topography, it was paramount to have a robust high resolution and accurate
165 Digital Elevation Model (DEM) for the study region. To avoid the uncertainties that most global
166 DEMs are plagued with and overcome the problem of different DEM origins on the French and
167 Italian sides of the MBM, we built our own DEM. As part of the CNES *Kalideos Alps* project,
168 stereoscopic sub-meter resolution optical images from the Pleiades constellation were acquired.
169 Using the pair of stereo panchromatic images (25/08/2019), a 4 m resolution DEM was computed
170 using the Ames Stereo Pipeline (ASP), an open-source processing chain developed by Shean et al.
171 (2016). ASP uses the rational polynomial coefficients provided with the Pleiades images,
172 eliminating the requirement of many high accuracy ground control points (GCPs). Parameters used
173 for the processing were kept the same as Marti et al. (2016). ASP generates a point cloud with
174 elevation values, then gridded into a 4 m resolution DEM using the 'point2DEM' function. The
175 robustness and efficiency of the ASP processing chain for Pleiades data processing based on GCPs
176 has been documented previously by Berthier et al. (2007, 2014). The second part of the processing
177 involves accurately co-registering the newly built DEM with an existing reference DEM of high
178 precision and accuracy. For this purpose, we used the automatic DEM co-registration methodology
179 given by Nuth and Kääb (2011). As a 'reference', we used a 2 m LiDAR DEM (Fig. 2a) built by
180 the *Institut des Géosciences de l'Environnement* (IGE) to co-register the 'source' 4 m Pleiades
181 DEM (Fig. 2b) generated in the previous step. We used the RGI (Randolf Glacier Inventory)
182 glacier contours, forest extensions and manually delineated polygons to mask non-stable areas like



183 glacier and forest regions with an open-source script (<https://github.com/dshean/demcoreg>). After
184 masking the non-stable areas, only stable areas were used for the co-registration process. The
185 source DEM was then shifted (translation only) using the corresponding shift values (in meters)
186 for x, y and z. A precisely co-registered, high-resolution, robust 4 m DEM was obtained at the end
187 of the processing. We used this DEM to compute topographic parameters like slope, aspect,
188 curvature, elevation, TRI, MARST and direct solar radiation.

189

190

191 **3.2 Optical aerial and satellite images**

192

193 This study relies on high-resolution aerial and satellite images (Table 1). Working with data from
194 different sources allows us to tap into the wealth of data for comparison. Spanning over seven
195 decades and covering the whole MBM ortho-images for 1952, 2001 and 2015 at 0.2 m resolution
196 were downloaded from *Géoportail* IGN (French *Institut national de l'information géographique*
197 *et forestière*), while the panchromatic and XS images from SPOT 6 and Pleiades at 2.2 m and 0.5
198 m respectively were downloaded from the *Kalideos Alps* website. Considering the small
199 dimensions of the ice bodies, we could only work with high-resolution optical images covering
200 the entire MBM. We were thus limited by only one set of excellent quality images for 1952 and
201 2001, as very high-resolution images for this study period were not available from any other
202 source. For 2012 and 2019, we have data from multiple sources to deal with the problems
203 associated with the lack of coverage, cloud cover, illumination, shadow, and seasonal snow cover
204 that make visual interpretation difficult. To avoid overestimating the extent of IAs, it was
205 preferable to have all images acquired at the end of the summer period (late August or early
206 September). Considering that our optical images come from many sources, it is necessary to
207 accurately co-register all images. We used the automatic 'image to image' co-registration tool in
208 ENVI 5.6. The process includes locating and matching several feature points called tie points in a
209 'reference' image and a 'warped' image selected for co-registration. Here, we used the Pleiades
210 panchromatic image of 2019 as a reference, and all the warped images were accordingly co-
211 registered. Both coarse and fine co-registration procedures were performed, and the co-registration
212 process was stopped when the RMSE values achieved were less than half the pixel resolution of



213 the warped image based on the recommendations of Han and Oh (2018). A more detailed
214 description of the co-registration process was discussed in Kaushik et al. (2021).

215

216 **3.3 Meteorological data**

217

218 To explore the correlated variations in the surface area of IAs with the changing climate, we need
219 to build proxies to define accumulation and ablation phases. A similar study for 6 IAs was
220 performed by Guillet and Ravanel (2020); we aim to test the validity of their results with a more
221 extensive database (*c.*200 IAs) in the entire MBM. Since the IAs are spread across different
222 elevation ranges, we test the results using the SAFRAN reanalysis product (Vernay et al., 2019)
223 that produces gridded datasets of temperature, precipitation, wind speed, and other meteorological
224 variables at an hourly time step. These data are available as NetCDF files from 1958 for all the
225 French massifs, at every 300 m elevation belts, at 0, 20, 40° slopes, and for all eight aspects (N,
226 NE, E, SE, S, SW, W, NW).

227 For our analysis, we used weather records from the Col du Grand Saint Bernard (GSB), located
228 close to the MBM at 2469 m a.s.l., and from the Aiguille du Midi (AdM) cable-car station (3810
229 m a.s.l.). GSB represents a similar climatological regime as the MBM, and the weather records are
230 available for an extended period starting from the 1860s. Such long-term weather records are not
231 available from any weather station in the MBM. Since all IAs are present at elevations above the
232 elevation of the GSB weather station, it was necessary to transform the weather records to an
233 elevation closer to the average elevation range of the IAs. For this reason, it was necessary to
234 transform the data from the GSB station using the weather records from the AdM weather station
235 (data available since 2007). Guillet and Ravanel (2020) found a strong correlation between the
236 monthly averaged AdM and GSB temperature records and were able to transform the GSB
237 temperatures using a linear model:

238

$$239 \quad T_{AdM} = \alpha T_{GSB_i} + \beta + r_i, \quad (1)$$

240

241 where $\alpha = 0.87$ (slope), $\beta = -7.7^\circ \text{C}$ (intercept) and r (residuals) with zero mean.

242 No transformation for the precipitation values was performed as this relation is tough to establish
243 and not always linear (Smith, 2008). Hence, the original GSB precipitation values were used for



244 the analysis. Using these weather records, Guillet and Ravanel (2020) found a robust correlation
245 between ablation and accumulation proxies and the surface area change of 6 IAs. We used the
246 same datasets to test for similar potential relationships for *c.* 200 IAs, and the results are shown in
247 Sect. 5.5.

248 Since the previous study involved a small number of IAs, the disparity arising from elevation
249 differences of IAs (in turn, the temperature and precipitation coming from weather stations at a
250 fixed elevation) could have been minimized or not well represented. We decided to use the
251 SAFRAN reanalysis product and checked for similar potential relationships of climate variables
252 with the surface area change of IAs. The first problem we encountered was that the SAFRAN data
253 starts from 1958, while our first images date from 1952. Therefore, for comparison, it was essential
254 to interpolate the missing data for the six years before 1958 (Fig. 3). Like the previous
255 methodology, we looked for a linear relationship between the SAFRAN temperature data (at 2400
256 m a.s.l. elevation belt) and the GSB temperature data. We again found a strong correlation between
257 the two datasets (Fig. 4) which helped us transform the data using:

258

$$259 \quad T_{\text{SAFRAN2400}} = \alpha T_{\text{GSB}_i} + \beta + r_i, \quad (2)$$

260

261 where $\alpha = 1.01$ (slope), $\beta = -1.35^\circ \text{C}$ (intercept) and r (residuals) with zero mean.

262 For the SAFRAN data estimated (2400 m a.s.l.) from 1952, it was essential to extrapolate the data
263 for all elevation bands. We used a standard gradient of $-0.53^\circ \text{C}/100 \text{ m}$ increase of elevation based
264 on the observations of Magnin et al. (2015) for the MBM.

265 As previously stated, a similar relationship for precipitation is tough to establish. Hence, for the
266 analysis, we used the SAFRAN precipitation data from 1958 and extrapolated the precipitation
267 values from the GSB weather station to all elevation bands of SAFRAN data before 1958 (six
268 years, up to 1952). However, taking a cue from the previous study of Guillet and Ravanel (2020),
269 we expect the impact of this to be insignificant when considering the results over seven decades.

270

271

272 **4 Methods**

273

274 **4.1 Mapping the surface area of IAs from high-resolution satellite images**



275

276 IAs boundaries were manually delineated/digitized by the first author of this paper to maintain
277 data consistency in a GIS environment for 1952, 2001, 2012 2019. The problem of seasonal snow,
278 which can lead to an overestimation of surface areas, was avoided by using images at the end of
279 the ablation period. The differentiation of IAs from other snow/ice bodies relies on the slope angle
280 (we only consider ice bodies on slopes $> 40^\circ$ to be IAs) and whether they are thick enough to
281 deform under their own weight and show movement like in the case of hanging glaciers. The slope
282 mask to remove areas with slopes $< 40^\circ$ was built in ArcGIS 10.6 using the Pleaides DEM.
283 Figure 5 shows the variations in the surface areas of IAs over the study period. It also highlights
284 the importance of high-resolution images because of the small dimensions of the ice bodies we are
285 studying.

286

287 **4.2 Generation of topo-climatic parameters**

288

289 The relative area loss of IAs for three time periods, *i.e.* 1952 to 2001, 2001 to 2012 and 2012 to
290 2019, is analyzed with all topographic factors. The area loss is expressed as a relative percentage
291 of the area lost between the first observation and the next. Authors like Salerno et al. (2017) have
292 also used absolute values, but for our study, this would not give a fair estimation for the analysis
293 as it generates a bias based on the size of IAs. The factors we considered for our analysis are
294 elevation, slope, aspect, curvature, TRI, direct solar radiation (all estimated in ArcGIS 10.6), mean
295 annual rock surface temperature (MARST), and size of the IAs. The topographic parameters are
296 generated using the 4 m Pleaides DEM (see Sect. 3.1.1).

297

298 **Direct solar radiation:**

299 Direct solar radiation (DSR) measures the potential total insolation across a landscape or at a
300 specific location. The intensity of solar radiation received at the surface mainly depends on the
301 latitude and time of the year. On a local scale, components such as topographic shading, slope, and
302 aspect also control the radiation distribution (Olson and Rupper, 2019). The viewshed algorithm
303 was run based on a uniform sky and a fixed atmospheric transmissivity value of 1. Sabo et al.
304 (2016) showed the application of these algorithms in areas of rough topography. The total DSR



305 (DSR_{tot}) for a given location is calculated as the sum of the DSR (Dir_{θ,α}) from all the sun sectors
306 (calculated for every sun position at 30 minutes intervals throughout the day and month for a year):

307
$$DSR_{tot} = \sum DSR_{\theta,\alpha} \quad (3)$$

308

309 The direct solar radiation (Dir_{θ,α}) with a centroid at zenith angle (θ) and azimuth angle (α) is
310 calculated using the following equation:

311

312
$$DSR_{\theta,\alpha} = S_{Const} * (\beta^{m(\theta)}) * SunDur_{\theta,\alpha} * SunGap_{\theta,\alpha} * \cos(AngIn_{\theta,\alpha}), \quad (4)$$

313

314 where S_{Const} is the solar constant with a value of 1367 W/m², β is the transmissivity of the
315 atmosphere (averaged over all wavelengths) for the shortest path (in the direction of the zenith),
316 m(θ) is the relative optical path length, measured as a proportion relative to the zenith path length,
317 SunDur_{θ,α} is the time duration represented by the sky sector, SunGap_{θ,α} is the gap fraction for the
318 sun map sector and AngIn_{θ,α} is the angle of incidence between the centroid of the sky sector and
319 the axis normal to the surface.

320 The final map of DSR is the sum of values calculated at an hourly time step for every pixel, as per
321 the resolution of the DEM used. The values of solar radiation are given in W/m². Higher values
322 for solar radiation indicate higher insolation, while lower values suggest low insolation. We prefer
323 DSR over the aspect for our analysis to avoid bias due to local shading on sun-exposed faces,
324 considering the slope angle associated with the aspect.

325

326 **Elevation:**

327 Elevation strongly influences the climatic conditions within the same region, significantly altering
328 the precipitation, temperature, and wind regime even at a local scale. Generally, higher elevations
329 receive more precipitation and experience lower temperatures and higher wind speeds. In the case
330 of IAs at high elevations, with Fig. 3, we showed that they receive more precipitation inputs and
331 experience lower air temperatures. Hence regions at higher elevations, especially above the ELA,
332 should favour more accumulation than ablation. However, wind-driven snow at higher elevations
333 does not readily accumulate on steep slopes. Some IAs may take advantage of the leeward
334 conditions at lower elevations and sustain for more extended periods. Similar results for large



335 glaciers have previously been reported by Bhambri et al. (2011) or Pandey and Venkataraman
336 (2013).

337

338 **Mean slope:**

339 Slope angle strongly influences ice velocities of glaciers, mass flux, and the hydrology of the
340 mountain environments. Its influence on avalanche transport of snow over the glacier surface has
341 been discussed previously (*e.g.*, Oerlemans, 1989; Hoelzle et al., 2003; DeBeer and Sharp, 2009).

342 Numerous studies have also reported that slope is the single most crucial terrain parameter that
343 controls glacier responses to climate change (Furbish and Andrews, 1984; Oerlemans et al., 1998;
344 Jiskoot et al., 2009; Scherler et al., 2011). Terrain slope has a strong influence on the accumulation
345 rates in rugged terrains. On steep slopes, accumulation occurring in the temperature range of -5 -
346 0° C can accumulate on steep slopes. Slope likewise plays a key role when calculating other terrain
347 parameters and indices.

348

349 **Mean annual rock surface temperature:**

350 MARST estimates the average annual temperature of the rock surface governed mainly by the
351 incoming shortwave solar radiation (PISR) and the mean annual air temperature (MAAT). The
352 method for estimating MARST is described by Boeckli et al. (2012) and Magnin et al. (2019). The
353 estimation is based on a multiple linear regression model with the form:

354

355
$$Y = \alpha + \sum_{i=1}^k \theta_i X^i + \varepsilon, \tag{5}$$

356

357 where Y is the value for MARST, α is the intercept term, $\theta_i X^i$ represents the model's k variables
358 (PISR and MAAT) and their respective coefficients, and ε residual error term distributed equally
359 with the mean equal to 0 and the variance $\sigma^2 > 0$. For predicting the values of MARST in steep
360 slopes, we use the equation:

361

362
$$\text{MARST}_{(\text{pred})} = \alpha + \text{PISR} * b + \text{MAAT} * c, \tag{6}$$

363



364 where α is the $MARST_{pred}$ value when PISR and MAAT are equal to 0, and b and c are the
365 respective coefficients of PISR and MAAT at measured RST positions. These coefficients were
366 calibrated by Boeckli et al. (2012) (rock model 2) for the entire European Alps using a set of 53
367 MARST measurement points. The MAAT of the 1961-1990 period was used to calculate MARST,
368 representing a steady state.

369 The values for MARST are calculated in °C and, for our study region, range from -12 to 10°C.

370 MARST is also an important criterion to check for the very likely presence of permafrost below
371 the IAs, which likely allows the formation and existence of IAs.

372

373 **Topographic Ruggedness Index:**

374 The topographic Ruggedness Index (TRI) measures the ruggedness of the landscape. TRI was
375 calculated based on the methodology proposed by Sappington et al. (2007). It is calculated as a 3-
376 dimensional dispersion of vectors (x, y, z components) normal to the grid cells considering the
377 slope and aspect of the cell. The magnitude of the resultant vector in a standardized form (vector
378 strength divided by the number of cells in the neighbourhood) measures the ruggedness of the
379 landscape. Higher values of TRI thus suggest a more rugged and sporadic terrain, which could
380 block the downward movement of the snow and subsequently lead to the formation of a consistent
381 weak layer, which can destabilize the snowpack and lead to small avalanches resulting in mass
382 wasting (Schweizer, 2003). Since IA surfaces are smooth, the TRI values calculated at the surface
383 of the IA is always low. Hence, we consider the TRI values by taking a buffer of 20 m around the
384 IA boundary delineated for the first observation (1952). The mean TRI value from this buffer is
385 considered for our analysis.

386

387 **Curvature:**

388 Curvature, estimated as a second derivative of the surface, defines the shape of the slope. Curvature
389 is considered an essential factor because it can define accumulation or ablation rates for a surface.
390 It is also considered a significant contributory factor for avalanches (Snehmani et al., 2014).
391 Generally, two types of curvature profiles are known, plan and profile. For our analysis, we only
392 used the profile curvature as it defines the shape of the slope in the steepest direction. From a
393 theoretical point of view, erosion processes prevail in convex (negative values) profile curvature
394 locations, while deposition is predominant in concave (positive values) profile curvature locations.



395 The values for the curvature define how strongly convex (lower negative values) or concave
396 (higher positive values) the slope is. That is why curvatures can be considered an essential role in
397 the accumulation and ablation rates of a glacier or ice body. Like TRI, the IAs tend to show flat
398 curvature profiles if we consider their surface. Hence, we estimate the curvature values around the
399 same buffer as the TRI and use this for further analysis.

400

401

402 **4.3 Proxies for ablation and accumulation**

403

404 To eventually correlate changes in surface area of IAs with the changing climate, we use the
405 temperature and precipitation data from the transformed AdM weather records and SAFRAN
406 reanalysis product (see Sect. 3.1.3) to build proxies for accumulation and ablation. The proxy for
407 ablation was built by estimating the annual sum of positive degree-days (PDD), computed from
408 the normal probability distribution centred around the mean monthly temperature. Estimation of
409 the PDD is based on the empirical relation, which states that the melting rate is proportional to the
410 surface-air temperature excess above 0°C. Several methods for estimating the PDD have been
411 proposed by Braithwaite and Olesen (1989), Braithwaite (1995), and Hock (2003). However, the
412 method proposed by Calov and Greve (2005) also accounts for stochastic variations in temperature
413 during the computation of PDD. The formula for the estimation of the PDD using this method is
414 given by:

415

$$416 \quad \text{PDD} = \int_0^A dt \left[\frac{T_{ac}^2}{\sqrt{2\pi}} \exp\left(-\frac{T_{ac}}{2\sigma^2}\right) + \frac{T_{ac}}{2} \operatorname{erfc}\left(-\frac{T_{ac}}{\sqrt{2}\sigma}\right) \right] \quad (7)$$

417

418 T_{ac} is the annual temperature cycle (in °C), σ is the standard deviation of the temperature from the
419 annual cycle, $A = 1$ year, and erfc is the conventional error function built-in in all programming
420 languages.

421 After computing the PDD, we calculate the cumulative PDD (CPDD) by taking the sum of all the
422 annual PDD values for each observation period (*i.e.* 1952-2001, 2001-2012 and 2012-2019). This
423 value of CPDD is then used as a proxy for ablation (Braithwaite and Olesen, 1989; Vincent and
424 Vallon, 1997).



425 The calculation of the proxy for accumulation is more tricky because we only consider the yearly
426 sum of precipitation occurring at a temperature between -5 and 0°C , as only snowfall within this
427 temperature range is believed to accumulate/adhere to steep slopes (Kuroiwa et al., 1967; Guillet
428 and Ravanel, 2020; Eidevåg et al., 2022). The temperature-dependent indicator function can be
429 written in the following form:

430

$$\chi_i(T, (t)) = \begin{cases} 1 & \text{if } -5^{\circ}\text{C} \leq T(t) \leq 0^{\circ}\text{C} \\ 0 & \text{otherwise} \end{cases} \quad (8)$$

432

433

434

435 **4.4 Surface area model**

436

437 Using the proxy for ablation and accumulation, Guillet and Ravanel (2020) proposed a surface
438 area model to estimate the differences in the surface areas of IAs between different time steps due
439 to the time-integrated changes in climate forcing parameters. The main goal is to look for a
440 potential linear relationship between climate variables and the changes in surface areas of IAs,
441 using a multivariate regression model. The equation for the model can be written as:

442

$$443 \quad S_m(t) = S(t_0) - \int_{t_0}^t (\alpha_1 CPDD(t) - \chi_i(T(t))\alpha_2 A(t))dt + \beta + \varepsilon(t) \quad (9)$$

444

445 where $S_m(t)$ corresponds to the modelled surface area at time t ; similarly, $CPDD(t)$ and $A(t)$
446 represent the proxies for ablation and accumulation; $S(t = 0)$ is the first available measurement; α_1
447 and α_2 are the coefficients of linear regression, β is the intercept, and ε the residual. $\chi(T, t)$ accounts
448 for precipitation occurring in the $[-5^{\circ}\text{C}, 0^{\circ}\text{C}]$ temperature range and is given by the temperature-
449 dependent indicator function given in equation (5). The area of IAs at each time step was calculated
450 using the surface area model (with the temperature and precipitation proxies), and we hereafter
451 refer to this area as modelled area. The measured area is the surface area we delineated using the
452 high-resolution optical images.

453

454 **4.5 Uncertainty estimations**

455



456 Since this study uses data from different sources and periods, uncertainties of different origins
457 might have been introduced to delineate the IA boundaries. A good estimation of these
458 uncertainties is thus crucial to have a fair estimation of the significance of the results (Racoviteanu
459 et al., 2008; Shukla and Qadir, 2016; Garg et al., 2017). Some sources of uncertainty in this study
460 could arise from (1) errors inherent to the aerial images and satellite-derived datasets, (2) errors
461 resulting from inaccurate co-registration of data from various sources, (3) errors produced while
462 generating the high-resolution DEM from stereo images, and (4) conceptual errors linked with
463 defining the boundaries of IAs in all images. Quantifying the errors inherent to the processing of
464 all datasets used is challenging, and this is out of the scope of this paper. A detailed accuracy
465 assessment of the DEM generation and co-registration process is provided in Sect. 5.1 and 3.2,
466 respectively. The quantification of errors resulting from the manual delineation of IA boundary is
467 also challenging, but we have previous guidelines from Paul et al. (2017) for the quality and
468 consistency assessment of manual delineations.

469 One way to assess the area uncertainty is to perform multiple digitizations of the same area and
470 calculate the mean area deviation (MAD), taking the first digitization as a reference (Meier et al.,
471 2018). Considering this, the first author performed multiple digitizations (three times) for 50 IAs
472 on images from 1952, 2001, 2012 and 2019, considering different challenges associated with aerial
473 and satellite images like shadow and illumination. The MAD gives an uncertainty estimate in
474 percentage considering multiple digitizations taking the first digitization as a reference. MAD
475 provides a percentage estimate of how the final area calculated varies across multiple digitizations
476 for each polygon. MAD values are affected by the size of the polygon manually digitized.
477 Previously, authors like Paul et al. (2013), Fischer et al. (2014) and Pfeffer et al. (2014) have
478 reported an increase in the uncertainty of manual digitizations with a decrease in the size of the
479 polygons. With this in mind, we also digitized IAs of different sizes ranging from 0.001 km² to
480 0.01 km².

481

482

483 **5 Results and discussions**

484

485 **5.1 Accuracy of the DEM**

486



487 Figure 6a shows the stable surfaces (after eliminating glacier boundaries, trees, and forests) we
488 used for our co-registration process and fig. 6b displays the difference in elevation between the
489 reference DEM and the source DEM before co-registration. Figure 6c presents the results after the
490 co-registration process considering all the surfaces (stable and non-stable), and fig. 6d shows the
491 difference considering only the stable areas after masking out non-stable areas using the glacier
492 boundaries provided by the RGI. The source DEM was translated using the corresponding shift
493 values $x = -5.03$ m, $y = 6.00$ m, and $z = 3.22$ m

494 The distribution of errors can be visualized by a histogram of the sampled errors, where the number
495 of errors (frequency) within certain predefined intervals is plotted (Höhle and Höhle, 2009). Figure
496 7 shows the histogram of the errors Δh (elevation difference between the reference and source
497 DEM) in meters for the stable areas. The accuracy estimates before and after the co-registration is
498 shown by the normalized median absolute deviation (nmad) and the median value calculated
499 together. As can be seen, the nmad and median values before the co-registration process for stable
500 areas were 5.16 and -5.06, respectively. After the co-registration process, the value dropped to
501 1.98 for the nmad and -0.14 for the median value. This suggests a good correlation between the
502 high-resolution LiDAR DEM used as a reference and the Pleiades DEM we built.

503

504 **5.2 Total area loss of ice aprons in the Mont-Blanc massif over seven decades**

505

506 The total area of IAs mapped in 1952 was 7.932 km². It dropped to 5.915 km² in 2001. The surface
507 area further dropped to 4.919 km² in 2012 and then to 4.21 km² in 2019 (Figure 8). This implies
508 that from 1952 to 2019, IAs have lost ~47 % of their original area in 67 years. It corresponds to an
509 average surface area loss of 0.78 km² per decade. However, the percentage area loss from 1952 to
510 2001 was ~26 % compared to ~31 % from 2001 to 2019. This is an alarming rate: IAs have lost
511 more relative areas during the 18 recent years compared to the previous 50 years (before 2001).
512 The rate of surface area loss is also disconcerting because, compared to the glaciers in the MBM,
513 the IAs are losing their area at a higher rate (~24 % for glaciers from the end of LIA till 2008,
514 according to Gardent et al., 2014). The small size of IAs seems to make them more vulnerable to
515 global warming than large glaciers. Also, the effects of local topography may be more pronounced
516 in the case of IAs than for large glaciers. Figure 9 shows the MAD values for 50 IAs in 1952, 2001,
517 2012 and 2019. We did not observe an increase in MAD values with decreasing size of the IAs,



518 mainly because the number of samples we used is comparatively less than that in the previous
519 studies. Overall, the mean MAD observed for all years was $\pm 6.4\%$. The MAD for the IAs digitized
520 on the orthophotos from 1952 was $\pm 6.68\%$, while for 2001, it was $\pm 7.2\%$. The MAD for 2012
521 and 2019 was $\pm 6.32\%$ and $\pm 5.50\%$, respectively.

522

523 **5.4 Influence of the local topography and other factors on the area loss of IAs**

524

525 Each parameter, as described in Sect. 4.2 was individually regressed with the relative area loss of
526 IAs for the three periods, and their influence was assessed by the coefficient of determination (R^2)
527 and Pearson's r-value.

528 A joint analysis of the surface area lost by the IAs and the direct solar radiation reveals a strong
529 correlation between the values of DSR and the relative surface area loss of IAs for all the three-
530 time periods (1952-2001, 2001-2012 and 2012-2019) (Fig. 10a; Table 2). IAs that receive more
531 radiation from the sun throughout the year lose their surface area faster than those that receive less
532 DSR (Oerlemans and Klok (2002); Mölg (2004); Johnson and Rupper (2020)). Incoming solar
533 radiation is also an essential component of all surface energy and mass balance models. However,
534 this is the first evidence of the potential negative impact of solar radiation on small ice bodies like
535 IAs. Our previous analysis with the climate variables in Sect. 3.3 indicated a potential relationship
536 between the elevation and the surface area loss of IAs. This is somewhat statistically significant
537 from the regression analysis, as we found a negative correlation between the surface area loss and
538 the mean elevation of the IAs (Fig. 10b; Table 2). IAs present at lower elevations are potentially
539 subject to intense degradation and lose their surface area faster than those at higher elevations. The
540 correlation is not particularly strong since, on a more local scale, other topographic factors also
541 play a critical role in the surface area variations of IAs. However, elevation seems to be particularly
542 the single dominant causative factor compared to other topographic factors in affecting the
543 behaviour of IAs to the changing climate. Elevation strongly influences climatic conditions
544 (temperature, precipitation, and wind speeds) and permafrost; this likely strongly influences the
545 durability of IAs in the context of changing climate. Hantel et al. (2012) suggested that the median
546 summer snowline for the Alps to be at 3083 ± 121 m a.s.l. (1961 – 2010), while Rabatel et al.
547 (2013) documented the regional ELA at 3035 ± 120 m a.s.l. (1984 – 2010). Previous authors further
548 described the rising of the ELA to 3250 ± 135 m a.s.l. during the 2003 heatwave. Subsequent



549 heatwaves of 2006, 2015 and 2019 would have likely resulted in similar scenarios (Hoy et al.,
550 2017). Since 87.5 % of the total IAs mapped (423 in total) exist in elevations above 3100 m a.s.l.
551 (Kaushik et al., 2021), the rising of the ELA in future climate scenarios leads to more IAs falling
552 at risk of fast degradation and disappearance. An example of this is the case of the IA on the north
553 face of Aiguille des Grands Charmoz (3445 m a.s.l.), which completely disappeared during the
554 2017 summer heatwave (Guillet and Ravanel, 2020).

555 In addition, we found a moderate positive correlation between the average MARST values and the
556 surface area loss of IAs. The correlation observed was not very significant compared to the
557 previous two factors. It indicates that the effect of rock surface temperatures on the area loss of
558 IAs is not strong on a regional scale, but this could still prove significant on a more local scale.
559 (Fig. 10c; Table 2). However, this relationship needs to be examined in a more site-specific and
560 localized area as it was not exposed glaringly for the large sample size and distributed dataset used
561 for our analysis. We also observed that the correlation degree was higher for a more extensive
562 observation period (1952-2001) than for shorter periods. This could suggest that the influence of
563 rock surface temperatures potentially becomes more prominent with a more extensive observation
564 period. As suggested by Guillet et al. (2021), IAs are cold ice bodies that exist predominantly on
565 permafrost-affected rock walls. They further reported temperatures $<0^{\circ}\text{C}$ at the base of the ice core
566 taken from the IA on the north face of Triangle du Tacul (3970 m a.s.l.). Heating from rock surfaces
567 is predominantly the cause of permafrost degradation, which further affects mountain slope
568 stability leading to an increased rock mass wasting (Magnin et al., 2017). Cold surfaces
569 demonstrate more ice cohesion with the underlying surfaces, while a rise in surface temperatures
570 decreases basal cohesion, increasing the sliding process and leading to more ice flow (Deline et
571 al., 2015). Thus, it is likely that underlying permafrost conditions aid the sustainability of IAs in
572 the long term, and an increase in rock surface temperatures around IAs could result in IAs losing
573 mass more rapidly.

574

575

576 Kaushik et al. (2021) further showed that most IAs exist in extremely rugged terrains: 51 % of the
577 total IAs mapped exist in the TRI's high and very high ruggedness class, while only 8 % exist in
578 the low ruggedness. Thus, comparing the terrain ruggedness to the area loss of IAs makes sense
579 since the topography around the snow/ice bodies can critically influence their stability (Deline et



580 al., 2015). Increasing terrain ruggedness is associated with slope instability and further ice volume
581 loss. However, a similar analysis of IA area loss with the TRI showed a weak positive correlation
582 (Fig. 10d; Table 2). An increase in TRI values (*i.e.* increase in terrain ruggedness) may result in
583 more ice area loss on a site-specific scale, but this relationship is hard to observe globally. Like
584 the results from the analysis with MARST, the strongest correlation was again observed for the
585 largest study period.

586

587 Further, like the TRI, we also found a weak correlation of the terrain slope and curvature with the
588 surface area loss of IAs. It is important to note that our criteria for selecting IAs already limit us
589 to areas with slope angles steeper than 40° (Fig.10e; Table 2). Previous analysis (Kaushik et al.,
590 2021) shows that most IAs in the MBM (83 %) lie at mean slopes between 40° and 65° . Increasing
591 slope steepness limits accumulation, while avalanches further scour away snow from the surface
592 of the IA, thus exposing the ice directly to the sun and wind (Vionnet et al., 2012). However, the
593 differences in slope angles of the IAs was not a dominant factor affecting the rates of area loss. A
594 plausible explanation for this could be that since we limit the slope criteria to more $>40^\circ$ and most
595 IAs lie in the range of 40 to 65° slope angles, the effect of terrain slope is not as well pronounced
596 as it could be between low ($< 15^\circ$) and extreme slopes ($>65^\circ$). Similar results were observed by
597 Li et al. (2011), as they observed very slight variations in area loss for small glaciers with
598 differences in slope. They suggested other local topographic factors could mitigate the effects of
599 slope in case of small ice/snow bodies.

600 Similarly, terrain curvature seems to have the most negligible impact (Fig. 10f; Table 2). As cited
601 in Sect. 4.2. previous studies may have shown that terrain curvatures could play an essential role
602 in the dynamics of glaciers, but this is not the case for IAs in the MBM.

603 We performed the last comparison between the relative surface area loss of IAs with their initial
604 area. Our results were similar to the one reported by Lopez et al. (2009) as we did not find any
605 correlation between the two quantities (Fig. 10g; Table 2). Although previous studies by Paul et
606 al. (2004), Jiskoot et al. (2009), and Garg et al. (2017) have shown the correlation between the size
607 of the ice/glacier bodies with the area loss, this is not evident in our case. Unlike previous studies,
608 which considered different glaciers ranging in size from less than a km^2 up to several hundred km^2 ,
609 IAs are small ice bodies (0.0005 km^2 to 0.2 km^2). Hence, it is plausible that the effect of IA size
610 related to area loss rate is not pronounced in our case. Similar results were shown by Lopez et al.



611 (2010), who analyzed 72 glaciers in South America, and reported no correlation between the
612 glacier length and the area loss of glaciers.

613

614

615 **5.5 Influence of changing climate on the area loss**

616

617 Figure 11 shows how the PDD increased over the years in the MBM. All elevations, except 4800
618 m a.s.l., show an increasing trend of PDD values from 1952 to 2019. Figure 12a presents the
619 correlation between the ratio of the mean measured surface area at time t , $S(t)$, to the initial area,
620 $S(t_0)$, with the ratio of the mean modelled surface area using the AdM transformed data to the
621 initial area for 2001 and 1952. We consider the ratio of $S(t)/S(t_0)$ as an indicator to estimate the
622 area loss between the two time periods. A high value of the ratio (*i.e.* value close to 1) in the present
623 context indicates that the relative surface area loss of IAs between the two periods is comparatively
624 less than that of IAs whose ratio is closer to 0. A value larger than 1 indicates an increase in the
625 surface area over time.

626 From the results, we do not see a strong correlation ($r = 0.73$) between the modelled area (from
627 AdM transformed climate data) and the measured area for the 200 IAs spread across the MBM
628 (Fig. 12a). However, the correlation improves significantly ($r = 0.86$) when we use the SAFRAN
629 data based on different elevations and remodel the surface area for each IA (Fig. 12b). This can be
630 seen from the values of R^2 , Pearson's r , RMSE and the p-value estimates from the T-test achieved
631 from both datasets (Table 3). The best-fitting line presents a slope of 1.0 and an intercept of 0.0.

632 Both figures show that IAs at lower elevations (blue to green colour and small tick size) generally
633 show lower ratios values than IAs at higher elevations (yellowish colours and bigger tick size).

634 This implies that the elevation of the IAs potentially plays a crucial role in their response to the
635 changing climate. Overall, the surface area of IAs has decreased throughout the massif from 1952
636 to 2001 except for 4 IAs, which showed an increase in surface area. All these 4 IAs are located at
637 the highest elevation band, which could favour the accumulation and growth of the IAs. The
638 results, however, reaffirm the proficiency of the proposed surface area model in predicting new IA
639 states from the accumulation and ablation proxies. Similar results were observed for the other two
640 time periods, *i.e.* 2001-2012 and 2012-2019, as seen in Table 3.



641 Our results indicate the strong influence of temperature and precipitation on the surface area
642 changes of IAs. The results raise further questions regarding the sensitivity of the IAs to extreme
643 weather events. Unfortunately, our sampling rate does not allow us to quantify the effects of
644 individual extreme weather events. Nevertheless, there is a strong argument in favour that these
645 events, especially in the past two decades, cause the IAs to lose mass more rapidly than in the
646 previous decades. As suggested by Meehl and Tebaldi, (2004), with an increase in the intensity
647 and frequency of extreme events in the coming decades, understanding the effects of climate
648 variables on the sensitivity of IAs is even more critical.

649 Further, several authors have previously also accounted for the variations in solar radiation in
650 mass-balance modelling studies (Huss et al., 2009; Thibert et al., 2018). Our results showed a
651 strong correlation of DSR with area change, making this argument stronger. However, since the
652 focus was to show the impact of climate variables separately, we preferred a temperature-index
653 model as a first approach. However, we expect solar radiation to play a significant role in the
654 sensitivity of ice aprons, and future studies on ice apron evolutions in the 21st century should
655 address this question.

656

657

658 **6. Conclusions**

659

660 This study makes the first attempt to understand the dynamics of IAs concerning the changing
661 climate and topographic factors at a regional scale. IAs are very small ice features but highly
662 critical components of the mountain cryosphere. Because of the difficulties associated with their
663 monitoring and relative unimportance to mountain hydrology, no studies solely based on their
664 evolution on a regional scale have been performed before. This paper presented an analysis of 200
665 IAs spread throughout the MBM and existing in different topographic settings better to understand
666 their dynamics in the context of climate warming. For this purpose, we accurately mapped the IAs
667 on very high-resolution aerial and satellite images available for 1952, 2001, 2012 and 2019. Using
668 our extensive database of IAs, we compared the total area variation of IAs for three periods.
669 Further, we also attempted to establish a relationship between the surface area lost by IAs with
670 climate forcing parameters (*i.e.* temperature and precipitation) and their associated topographic
671 parameters.



672

673 Some important outcomes are:

- 674 • Over the study period 1952-2019, IAs have lost their surface area at a very alarming rate.
675 The total area of IAs in MBM was 7.93 km² in 1952, which dropped to 5.91 km² in 2001,
676 to 4.91 km² in 2012, and at last to 4.21 km² in 2019 (~ 47% drop in total surface area in
677 less than three-quarters of a century).
- 678 • The observed rate of relative area loss in the last 18 years (~31 %) is more than the overall
679 area loss during the 48 previous years (1952-2001; ~ 26 %).
- 680 • Results from the analysis of IA surface area loss and climate forcing parameters
681 conclusively proved the strong impact of climate forcing parameters on the behaviour of
682 small ice bodies like IAs.
- 683 • Further analysis of IA surface area loss with different topographic parameters showed
684 possible strong links of some topographic factors with the area loss of IAs, while other
685 factors are not relevant, at least on a regional scale.
- 686 • The strongest correlation of IAs surface area loss was found with the DSR and elevation.
687 Other factors like MARST, TRI, and mean terrain slope could also play an important role
688 locally, but their effect is not significant regionally. Other factors like terrain curvature and
689 the size of the IAs were not found to impact the IA's surface area loss significantly.

690

691 Looking at the melting rate of IAs and the future predictions of global climate change, it is evident
692 that these small and critical ice bodies are most vulnerable to adverse impacts. It is hard to imagine
693 any of the IAs surviving the next few decades with increasing temperatures at the present and
694 future melting rates. The loss of IAs will thus be the loss of crucial glacial heritages and
695 playgrounds for the iconic practice of mountaineering. Hopefully, this study forms a basis to
696 encourage further studies on IAs.

697

698

699 **Author contributions:** SK designed the study and drafted the paper, which was revised by all co-
700 authors. LR and FM helped in data interpretation and analysis. YY and ET proofread the
701 manuscript and provided valuable inputs for improving the overall quality of the paper. DC
702 processed and provided the DEM used for the study.



703

704 **Data availability:** The ice apron inventory will be made available on demand.

705

706 **Competing Interests:** The authors declare that they have no conflict of interest.

707

708 **Acknowledgements:**

709 This research is part of the USMB *Couv2Glas* and *GPCLim* projects. Pleiades data were acquired
710 within the CNES *Kalideos-Alpes* project and successfully processed under the program "*Emerging*
711 *risks related to the 'dark side' Alpine cryosphere*". We also thank C. Vincent of the *Institut des*
712 *Géosciences de l'Environnement* (IGE) for providing the LiDAR DEM of the Argentière glacier
713 area.

714

715

716 **References:**

717

718 Barker, M. L.: Traditional Landscape and Mass Tourism in the Alps, *Geographical Review*, 72, 395,
719 <https://doi.org/10.2307/214593>, 1982.

720 Bauder, A., Funk, M., and Huss, M.: Ice-volume changes of selected glaciers in the Swiss Alps since the
721 end of the 19th century, *Ann. Glaciol.*, 46, 145–149, <https://doi.org/10.3189/172756407782871701>,
722 2007.

723 Benn, D. I. and Evans, D. J. A.: *Glaciers & glaciation*, 2nd ed., Hodder education, London, 2010.

724 Berthier, E., Arnaud, Y., Kumar, R., Ahmad, S., Wagnon, P., and Chevallier, P.: Remote sensing estimates
725 of glacier mass balances in the Himachal Pradesh (Western Himalaya, India), *Remote Sensing of*
726 *Environment*, 108, 327–338, <https://doi.org/10.1016/j.rse.2006.11.017>, 2007.

727 Berthier, E., Vincent, C., Magnússon, E., Gunnlaugsson, Á. P., Pitte, P., Le Meur, E., Masiokas, M., Ruiz, L.,
728 Pálsson, F., Belart, J. M. C., and Wagnon, P.: Glacier topography and elevation changes derived from
729 Pléiades sub-meter stereo images, *The Cryosphere*, 8, 2275–2291, [https://doi.org/10.5194/tc-8-2275-](https://doi.org/10.5194/tc-8-2275-2014)
730 2014, 2014.

731 Bhambri, R., Bolch, T., Chaujar, R. K., and Kulshreshtha, S. C.: Glacier changes in the Garhwal Himalaya,
732 India, from 1968 to 2006 based on remote sensing, *J. Glaciol.*, 57, 543–556,
733 <https://doi.org/10.3189/002214311796905604>, 2011.

734 Boeckli, L., Brenning, A., Gruber, S., and Noetzli, J.: Permafrost distribution in the European Alps:
735 calculation and evaluation of an index map and summary statistics, *The Cryosphere*, 6, 807–820,
736 <https://doi.org/10.5194/tc-6-807-2012>, 2012.



- 737 Bolch, T., Kulkarni, A., Kaab, A., Huggel, C., Paul, F., Cogley, J. G., Frey, H., Kargel, J. S., Fujita, K., Scheel,
738 M., Bajracharya, S., and Stoffel, M.: The State and Fate of Himalayan Glaciers, *Science*, 336, 310–314,
739 <https://doi.org/10.1126/science.1215828>, 2012.
- 740 Braithwaite, R. J.: Positive degree-day factors for ablation on the Greenland ice sheet studied by energy-
741 balance modelling, *J. Glaciol.*, 41, 153–160, <https://doi.org/10.3189/S0022143000017846>, 1995.
- 742 Braithwaite, R. J. and Olesen, O. B.: Calculation of Glacier Ablation from Air Temperature, West
743 Greenland, in: *Glacier Fluctuations and Climatic Change*, vol. 6, edited by: Oerlemans, J., Springer
744 Netherlands, Dordrecht, 219–233, https://doi.org/10.1007/978-94-015-7823-3_15, 1989.
- 745 Calov, R. and Greve, R.: A semi-analytical solution for the positive degree-day model with stochastic
746 temperature variations, *J. Glaciol.*, 51, 173–175, <https://doi.org/10.3189/172756505781829601>, 2005.
- 747 Cogley, J. G., Hock, R., Rasmussen, L. A., Arendt, A. A., Bauder, A., Braithwaite, R. J., Jansson, P., Kaser,
748 G., Möller, M., Nicholson, L., and Zemp, M.: Glossary of glacier mass balance and related terms,
749 <https://doi.org/10.5167/UZH-53475>, 2011.
- 750 Davies, B. J., Carrivick, J. L., Glasser, N. F., Hambrey, M. J., and Smellie, J. L.: Variable glacier response to
751 atmospheric warming, northern Antarctic Peninsula, 1988–2009, *The Cryosphere*, 6, 1031–1048,
752 <https://doi.org/10.5194/tc-6-1031-2012>, 2012.
- 753 De Angelis, H.: Hypsometry and sensitivity of the mass balance to changes in equilibrium-line altitude:
754 the case of the Southern Patagonia Icefield, *J. Glaciol.*, 60, 14–28,
755 <https://doi.org/10.3189/2014JoG13J127>, 2014.
- 756 DeBeer, C. M. and Sharp, M. J.: Topographic influences on recent changes of very small glaciers in the
757 Monashee Mountains, British Columbia, Canada, *J. Glaciol.*, 55, 691–700,
758 <https://doi.org/10.3189/002214309789470851>, 2009.
- 759 Deline, P., Gardent, M., Magnin, F., and Ravel, L.: The morphodynamics of the mont blanc massif in a
760 changing cryosphere: a comprehensive review, *Geografiska Annaler: Series A, Physical Geography*, 94,
761 265–283, <https://doi.org/10.1111/j.1468-0459.2012.00467.x>, 2012.
- 762 Deline, P., Gruber, S., Delaloye, R., Fischer, L., Geertsema, M., Giardino, M., Hasler, A., Kirkbride, M.,
763 Krautblatter, M., Magnin, F., McColl, S., Ravel, L., and Schoeneich, P.: Ice Loss and Slope Stability in
764 High-Mountain Regions, in: *Snow and Ice-Related Hazards, Risks and Disasters*, Elsevier, 521–561,
765 <https://doi.org/10.1016/B978-0-12-394849-6.00015-9>, 2015.
- 766 Dodson, R. and Marks, D.: Daily air temperature interpolated at high spatial resolution over a large
767 mountainous region, *Clim. Res.*, 8, 1–20, <https://doi.org/10.3354/cr008001>, 1997.
- 768 Eidevåg, T., Thomson, E. S., Kallin, D., Casselgren, J., and Rasmuson, A.: Angle of repose of snow: An
769 experimental study on cohesive properties, *Cold Regions Science and Technology*, 194, 103470,
770 <https://doi.org/10.1016/j.coldregions.2021.103470>, 2022.
- 771 Fischer, L., Käab, A., Huggel, C., and Noetzi, J.: Geology, glacier retreat and permafrost degradation as
772 controlling factors of slope instabilities in a high-mountain rock wall: the Monte Rosa east face, *Nat.*
773 *Hazards Earth Syst. Sci.*, 6, 761–772, <https://doi.org/10.5194/nhess-6-761-2006>, 2006.



- 774 Fischer, M., Huss, M., and Hoelzle, M.: Surface elevation and mass changes of all Swiss glaciers 1980–
775 2010, *The Cryosphere*, 9, 525–540, <https://doi.org/10.5194/tc-9-525-2015>, 2015.
- 776 Frans, C., Istanbuluoglu, E., Lettenmaier, D. P., Clarke, G., Bohn, T. J., and Stumbaugh, M.: Implications
777 of decadal to century scale glacio-hydrological change for water resources of the Hood River basin, OR,
778 USA: Hydrological Change in the Hood River Basin, *Hydrol. Process.*, <https://doi.org/10.1002/hyp.10872>,
779 2016.
- 780 Gardent, M., Rabatel, A., Dedieu, J.-P., and Deline, P.: Multitemporal glacier inventory of the French Alps
781 from the late 1960s to the late 2000s, *Global and Planetary Change*, 120, 24–37,
782 <https://doi.org/10.1016/j.gloplacha.2014.05.004>, 2014.
- 783 Garg, P. K., Shukla, A., Tiwari, R. K., and Jasrotia, A. S.: Assessing the status of glaciers in part of the
784 Chandra basin, Himachal Himalaya: A multiparametric approach, *Geomorphology*, 284, 99–114,
785 <https://doi.org/10.1016/j.geomorph.2016.10.022>, 2017.
- 786 Gilbert, A. and Vincent, C.: Atmospheric temperature changes over the 20th century at very high
787 elevations in the European Alps from englacial temperatures: EUROPEAN ALPS AIR TEMPERATURE
788 CHANGES, *Geophys. Res. Lett.*, 40, 2102–2108, <https://doi.org/10.1002/grl.50401>, 2013.
- 789 Gruber, S. and Haeberli, W.: Permafrost in steep bedrock slopes and its temperature-related
790 destabilization following climate change, *J. Geophys. Res.*, 112, F02S18,
791 <https://doi.org/10.1029/2006JF000547>, 2007.
- 792 Guillet, G. and Ravel, L.: Variations in surface area of six ice aprons in the Mont-Blanc massif since the
793 Little Ice Age, *J. Glaciol.*, 66, 777–789, <https://doi.org/10.1017/jog.2020.46>, 2020.
- 794 Guillet, G., Preunkert, S., Ravel, L., Montagnat, M., and Friedrich, R.: Investigation of a cold-based ice
795 apron on a high-mountain permafrost rock wall using ice texture analysis and micro-¹⁴C dating: a case
796 study of the Triangle du Tacul ice apron (Mont Blanc massif, France), *J. Glaciol.*, 1–8,
797 <https://doi.org/10.1017/jog.2021.65>, 2021.
- 798 Haeberli, W. and Gruber, S.: Global Warming and Mountain Permafrost, in: *Permafrost Soils*, vol. 16,
799 edited by: Margesin, R., Springer Berlin Heidelberg, Berlin, Heidelberg, 205–218,
800 https://doi.org/10.1007/978-3-540-69371-0_14, 2009.
- 801 Han, Y. and Oh, J.: Automated Geo/Co-Registration of Multi-Temporal Very-High-Resolution Imagery,
802 *Sensors*, 18, 1599, <https://doi.org/10.3390/s18051599>, 2018.
- 803 Hantel, M., Maurer, C., and Mayer, D.: The snowline climate of the Alps 1961–2010, *Theor Appl Climatol*,
804 110, 517–537, <https://doi.org/10.1007/s00704-012-0688-9>, 2012.
- 805 Hasler, A., Gruber, S., and Haeberli, W.: Temperature variability and thermal offset in steep alpine rock
806 and ice faces, *Frozen Ground*, <https://doi.org/10.5194/tcd-5-721-2011>, 2011.
- 807 Hock, R.: Temperature index melt modelling in mountain areas, *Journal of Hydrology*, 282, 104–115,
808 [https://doi.org/10.1016/S0022-1694\(03\)00257-9](https://doi.org/10.1016/S0022-1694(03)00257-9), 2003.



- 809 Hoelzle, M., Haeberli, W., Dischl, M., and Peschke, W.: Secular glacier mass balances derived from
810 cumulative glacier length changes, *Global and Planetary Change*, 36, 295–306,
811 [https://doi.org/10.1016/S0921-8181\(02\)00223-0](https://doi.org/10.1016/S0921-8181(02)00223-0), 2003.
- 812 Höhle, J. and Höhle, M.: Accuracy assessment of digital elevation models by means of robust statistical
813 methods, *ISPRS Journal of Photogrammetry and Remote Sensing*, 64, 398–406,
814 <https://doi.org/10.1016/j.isprsjprs.2009.02.003>, 2009.
- 815 Hoy, A., Hänsel, S., Skalak, P., Ustrnul, Z., and Bochníček, O.: The extreme European summer of 2015 in a
816 long-term perspective: EXTREME EUROPEAN SUMMER OF 2015 IN A LONG-TERM PERSPECTIVE, *Int. J.*
817 *Climatol.*, 37, 943–962, <https://doi.org/10.1002/joc.4751>, 2017.
- 818 Huss, M., Funk, M., and Ohmura, A.: Strong Alpine glacier melt in the 1940s due to enhanced solar
819 radiation, *Geophys. Res. Lett.*, 36, L23501, <https://doi.org/10.1029/2009GL040789>, 2009.
- 820 Immerzeel, W. W., Pellicciotti, F., and Bierkens, M. F. P.: Rising river flows throughout the twenty-first
821 century in two Himalayan glacierized watersheds, *Nature Geosci*, 6, 742–745,
822 <https://doi.org/10.1038/ngeo1896>, 2013.
- 823 IPCC, 2021: *Climate Change 2021: The Physical Science Basis. Contribution of Working Group I to the*
824 *Sixth Assessment Report of the Intergovernmental Panel on Climate Change*, 2021.
- 825 Jiskoot, H., Curran, C. J., Tessler, D. L., and Shenton, L. R.: Changes in Clemenceau Icefield and Chaba
826 Group glaciers, Canada, related to hypsometry, tributary detachment, length–slope and area–aspect
827 relations, *Ann. Glaciol.*, 50, 133–143, <https://doi.org/10.3189/172756410790595796>, 2009.
- 828 Johnson, E. and Rupper, S.: An Examination of Physical Processes That Trigger the Albedo-Feedback on
829 Glacier Surfaces and Implications for Regional Glacier Mass Balance Across High Mountain Asia, *Front.*
830 *Earth Sci.*, 8, 129, <https://doi.org/10.3389/feart.2020.00129>, 2020.
- 831 Kaushik, S., Ravel, L., Magnin, F., Yan, Y., Trouve, E., and Cusicanqui, D.: DISTRIBUTION AND
832 EVOLUTION OF ICE APRONS IN A CHANGING CLIMATE IN THE MONT-BLANC MASSIF (WESTERN
833 EUROPEAN ALPS), *Int. Arch. Photogramm. Remote Sens. Spatial Inf. Sci.*, XLIII-B3-2021, 469–475,
834 <https://doi.org/10.5194/isprs-archives-XLIII-B3-2021-469-2021>, 2021.
- 835 Kraaijenbrink, P. D. A., Bierkens, M. F. P., Lutz, A. F., and Immerzeel, W. W.: Impact of a global
836 temperature rise of 1.5 degrees Celsius on Asia’s glaciers, *Nature*, 549, 257–260,
837 <https://doi.org/10.1038/nature23878>, 2017.
- 838 Kuroiwa, D., Mizuno, Y., and Takeuchi, M.: Micromeritical properties of snow., 1, 751–772, 1967.
- 839 Laha, S., Kumari, R., Singh, S., Mishra, A., Sharma, T., Banerjee, A., Nainwal, H. C., and Shankar, R.:
840 Evaluating the contribution of avalanching to the mass balance of Himalayan glaciers, *Ann. Glaciol.*, 58,
841 110–118, <https://doi.org/10.1017/aog.2017.27>, 2017.
- 842 Li, K., Li, H., Wang, L., and Gao, W.: On the relationship between local topography and small glacier
843 change under climatic warming on Mt. Bogda, eastern Tian Shan, China, *J. Earth Sci.*, 22, 515–527,
844 <https://doi.org/10.1007/s12583-011-0204-7>, 2011.



- 845 Liu, T., Kinouchi, T., and Ledezma, F.: Characterization of recent glacier decline in the Cordillera Real by
846 LANDSAT, ALOS, and ASTER data, *Remote Sensing of Environment*, 137, 158–172,
847 <https://doi.org/10.1016/j.rse.2013.06.010>, 2013.
- 848 Magnin, F., Brenning, A., Bodin, X., Deline, P., and Ravel, L.: Modélisation statistique de la distribution
849 du permafrost de paroi : application au massif du Mont Blanc, *geomorphologie*, 21, 145–162,
850 <https://doi.org/10.4000/geomorphologie.10965>, 2015.
- 851 Magnin, F., Westermann, S., Pogliotti, P., Ravel, L., Deline, P., and Malet, E.: Snow control on active
852 layer thickness in steep alpine rock walls (Aiguille du Midi, 3842m.a.s.l., Mont Blanc massif), *CATENA*,
853 149, 648–662, <https://doi.org/10.1016/j.catena.2016.06.006>, 2017.
- 854 Magnin, F., Etzelmüller, B., Westermann, S., Isaksen, K., Hilger, P., and Hermanns, R. L.: Permafrost
855 distribution in steep rock slopes in Norway: measurements, statistical modelling and implications for
856 geomorphological processes, *Earth Surf. Dynam.*, 7, 1019–1040, [https://doi.org/10.5194/esurf-7-1019-](https://doi.org/10.5194/esurf-7-1019-2019)
857 2019, 2019.
- 858 Mahmoud Sabo, L., Mariun, N., Hizam, H., Mohd Radzi, M. A., and Zakaria, A.: Estimation of solar
859 radiation from digital elevation model in area of rough topography, *WJE*, 13, 453–460,
860 <https://doi.org/10.1108/WJE-08-2016-0063>, 2016.
- 861 Marti, R., Gascoin, S., Berthier, E., de Pinel, M., Houet, T., and Laffly, D.: Mapping snow depth in open
862 alpine terrain from stereo satellite imagery, *The Cryosphere*, 10, 1361–1380, [https://doi.org/10.5194/tc-](https://doi.org/10.5194/tc-10-1361-2016)
863 10-1361-2016, 2016.
- 864 Meehl, G. A. and Tebaldi, C.: More Intense, More Frequent, and Longer Lasting Heat Waves in the 21st
865 Century, *Science*, 305, 994–997, <https://doi.org/10.1126/science.1098704>, 2004.
- 866 Meier, W. J.-H., Griesinger, J., Hochreuther, P., and Braun, M. H.: An Updated Multi-Temporal Glacier
867 Inventory for the Patagonian Andes With Changes Between the Little Ice Age and 2016, *Front. Earth Sci.*,
868 6, 62, <https://doi.org/10.3389/feart.2018.00062>, 2018.
- 869 Mölg, T.: Ablation and associated energy balance of a horizontal glacier surface on Kilimanjaro, *J.*
870 *Geophys. Res.*, 109, D16104, <https://doi.org/10.1029/2003JD004338>, 2004.
- 871 Mourey, J., Marcuzzi, M., Ravel, L., and Pallandre, F.: Effects of climate change on high Alpine
872 mountain environments: Evolution of mountaineering routes in the Mont Blanc massif (Western Alps)
873 over half a century, *Arctic, Antarctic, and Alpine Research*, 51, 176–189,
874 <https://doi.org/10.1080/15230430.2019.1612216>, 2019.
- 875 Nuth, C. and Kääb, A.: Co-registration and bias corrections of satellite elevation data sets for quantifying
876 glacier thickness change, *The Cryosphere*, 5, 271–290, <https://doi.org/10.5194/tc-5-271-2011>, 2011.
- 877 Oerlemans, J. and Klok, E. J.: Energy Balance of a Glacier Surface: Analysis of Automatic Weather Station
878 Data from the Morteratschgletscher, Switzerland, *Arctic, Antarctic, and Alpine Research*, 34, 477–485,
879 <https://doi.org/10.1080/15230430.2002.12003519>, 2002.
- 880 Oerlemans, J. and Reichert, B. K.: Relating glacier mass balance to meteorological data by using a
881 seasonal sensitivity characteristic, *J. Glaciol.*, 46, 1–6, <https://doi.org/10.3189/172756500781833269>,
882 2000.



- 883 Oerlemans, J., Anderson, B., Hubbard, A., Huybrechts, P., Jóhannesson, T., Knap, W. H., Schmeits, M.,
884 Stroeven, A. P., van de Wal, R. S. W., Wallinga, J., and Zuo, Z.: Modelling the response of glaciers to
885 climate warming, *Climate Dynamics*, 14, 267–274, <https://doi.org/10.1007/s003820050222>, 1998.
- 886 Olson, M. and Rupper, S.: Impacts of topographic shading on direct solar radiation for valley glaciers in
887 complex topography, *The Cryosphere*, 13, 29–40, <https://doi.org/10.5194/tc-13-29-2019>, 2019.
- 888 Pandey, P. and Venkataraman, G.: Changes in the glaciers of Chandra–Bhaga basin, Himachal Himalaya,
889 India, between 1980 and 2010 measured using remote sensing, *International Journal of Remote Sensing*,
890 34, 5584–5597, <https://doi.org/10.1080/01431161.2013.793464>, 2013.
- 891 Paul, F., Kääb, A., Maisch, M., Kellenberger, T., and Haeberli, W.: Rapid disintegration of Alpine glaciers
892 observed with satellite data: DISINTEGRATION OF ALPINE GLACIERS, *Geophys. Res. Lett.*, 31, n/a-n/a,
893 <https://doi.org/10.1029/2004GL020816>, 2004.
- 894 Paul, F., Bolch, T., Briggs, K., Kääb, A., McMillan, M., McNabb, R., Nagler, T., Nuth, C., Rastner, P., Strozzi,
895 T., and Wuite, J.: Error sources and guidelines for quality assessment of glacier area, elevation change,
896 and velocity products derived from satellite data in the Glaciers_cci project, *Remote Sensing of
897 Environment*, 203, 256–275, <https://doi.org/10.1016/j.rse.2017.08.038>, 2017.
- 898 Rabatel, A., Letréguilly, A., Dedieu, J.-P., and Eckert, N.: Changes in glacier equilibrium-line altitude in the
899 western Alps from 1984 to 2010: evaluation by remote sensing and modeling of the morpho-
900 topographic and climate controls, *The Cryosphere*, 7, 1455–1471, [https://doi.org/10.5194/tc-7-1455-
901 2013](https://doi.org/10.5194/tc-7-1455-2013), 2013.
- 902 Racoviteanu, A. E., Arnaud, Y., Williams, M. W., and Ordoñez, J.: Decadal changes in glacier parameters
903 in the Cordillera Blanca, Peru, derived from remote sensing, *J. Glaciol.*, 54, 499–510,
904 <https://doi.org/10.3189/002214308785836922>, 2008.
- 905 Rafiq, M. and Mishra, A.: Investigating changes in Himalayan glacier in warming environment: a case
906 study of Kolahoi glacier, *Environ Earth Sci*, 75, 1469, <https://doi.org/10.1007/s12665-016-6282-1>, 2016.
- 907 Rastner, P., Prinz, R., Notarnicola, C., Nicholson, L., Sailer, R., Schwaizer, G., and Paul, F.: On the
908 Automated Mapping of Snow Cover on Glaciers and Calculation of Snow Line Altitudes from Multi-
909 Temporal Landsat Data, *Remote Sensing*, 11, 1410, <https://doi.org/10.3390/rs11121410>, 2019.
- 910 Ravelan, L., Deline, P., Lambiel, C., and Vincent, C.: Instability of a high alpine rock ridge: the lower arête
911 des cosmiques, mont blanc massif, france, *Geografiska Annaler: Series A, Physical Geography*, 95, 51–66,
912 <https://doi.org/10.1111/geoa.12000>, 2013.
- 913 Ravelan, L., Duvillard, P., Jaboyedoff, M., and Lambiel, C.: Recent evolution of an ice-cored moraine at
914 the G entianes P ass, V alais A lps, S witzerland, *Land Degrad. Develop.*, 29, 3693–3708,
915 <https://doi.org/10.1002/ldr.3088>, 2018.
- 916 Salerno, F., Thakuri, S., Tartari, G., Nuimura, T., Sunako, S., Sakai, A., and Fujita, K.: Debris-covered
917 glacier anomaly? Morphological factors controlling changes in the mass balance, surface area, terminus
918 position, and snow line altitude of Himalayan glaciers, *Earth and Planetary Science Letters*, 471, 19–31,
919 <https://doi.org/10.1016/j.epsl.2017.04.039>, 2017.



- 920 Sappington, J. M., Longshore, K. M., and Thompson, D. B.: Quantifying Landscape Ruggedness for Animal
921 Habitat Analysis: A Case Study Using Bighorn Sheep in the Mojave Desert, *Journal of Wildlife*
922 *Management*, 71, 1419–1426, <https://doi.org/10.2193/2005-723>, 2007.
- 923 Scherler, D., Bookhagen, B., and Strecker, M. R.: Spatially variable response of Himalayan glaciers to
924 climate change affected by debris cover, *Nature Geosci*, 4, 156–159, <https://doi.org/10.1038/ngeo1068>,
925 2011.
- 926 Schweizer, J.: Snow avalanche formation, *Rev. Geophys.*, 41, 1016,
927 <https://doi.org/10.1029/2002RG000123>, 2003.
- 928 Serquet, G., Marty, C., Dulex, J.-P., and Rebetez, M.: Seasonal trends and temperature dependence of
929 the snowfall/precipitation-day ratio in Switzerland: SNOWFALL/PRECIPIATION-DAY RATIO, *Geophys.*
930 *Res. Lett.*, 38, n/a-n/a, <https://doi.org/10.1029/2011GL046976>, 2011.
- 931 Shean, D. E., Alexandrov, O., Moratto, Z. M., Smith, B. E., Joughin, I. R., Porter, C., and Morin, P.: An
932 automated, open-source pipeline for mass production of digital elevation models (DEMs) from very-
933 high-resolution commercial stereo satellite imagery, *ISPRS Journal of Photogrammetry and Remote*
934 *Sensing*, 116, 101–117, <https://doi.org/10.1016/j.isprsjprs.2016.03.012>, 2016.
- 935 Shukla, A. and Qadir, J.: Differential response of glaciers with varying debris cover extent: evidence from
936 changing glacier parameters, *International Journal of Remote Sensing*, 37, 2453–2479,
937 <https://doi.org/10.1080/01431161.2016.1176272>, 2016.
- 938 Singh, V. P., Singh, P., and Haritashya, U. K.: *Encyclopedia of snow, ice and glaciers*, Springer, Dordrecht
939 London, 2011.
- 940 Smith, C. D.: The Relationship between Monthly Precipitation and Elevation in the Alberta Foothills
941 during the Foothills Orographic Precipitation Experiment, in: *Cold Region Atmospheric and Hydrologic*
942 *Studies. The Mackenzie GEWEX Experience*, edited by: Woo, M., Springer Berlin Heidelberg, Berlin,
943 Heidelberg, 167–185, https://doi.org/10.1007/978-3-540-73936-4_10, 2008.
- 944 Snehmani, Bhardwaj, A., Pandit, A., and Ganju, A.: Demarcation of potential avalanche sites using
945 remote sensing and ground observations: a case study of Gangotri glacier, *Geocarto International*, 29,
946 520–535, <https://doi.org/10.1080/10106049.2013.807304>, 2014.
- 947 Sorg, A., Huss, M., Rohrer, M., and Stoffel, M.: The days of plenty might soon be over in glacierized
948 Central Asian catchments, *Environ. Res. Lett.*, 9, 104018, [https://doi.org/10.1088/1748-](https://doi.org/10.1088/1748-9326/9/10/104018)
949 [9326/9/10/104018](https://doi.org/10.1088/1748-9326/9/10/104018), 2014.
- 950 Thibert, E., Dkengne Sielenou, P., Vionnet, V., Eckert, N., and Vincent, C.: Causes of Glacier Melt
951 Extremes in the Alps Since 1949, *Geophys. Res. Lett.*, 45, 817–825,
952 <https://doi.org/10.1002/2017GL076333>, 2018.
- 953 Triglav-Čekada, M. and Gabrovec, M.: Documentation of Triglav glacier, Slovenia, using non-metric
954 panoramic images, *Ann. Glaciol.*, 54, 80–86, <https://doi.org/10.3189/2013AoG62A095>, 2013.
- 955 Vernay, M., Lafaysse, M., Hagenmuller, P., Nheili, R., Verfaillie, D., and Morin, S.: The S2M
956 meteorological and snow cover reanalysis in the French mountainous areas (1958 - present),
957 <https://doi.org/10.25326/37>, 2019.



- 958 Vincent, C.: Influence of climate change over the 20th Century on four French glacier mass balances, *J.*
959 *Geophys. Res.*, 107, 4375, <https://doi.org/10.1029/2001JD000832>, 2002.
- 960 Vincent, C. and Vallon, M.: Meteorological controls on glacier mass balance: empirical relations
961 suggested by measurements on glacier de Sarennes, France, *J. Glaciol.*, 43, 131–137,
962 <https://doi.org/10.3189/S0022143000002896>, 1997.
- 963 Vionnet, V., Brun, E., Morin, S., Boone, A., Faroux, S., Le Moigne, P., Martin, E., and Willemet, J.-M.: The
964 detailed snowpack scheme Crocus and its implementation in SURFEX v7.2, *Geosci. Model Dev.*, 5, 773–
965 791, <https://doi.org/10.5194/gmd-5-773-2012>, 2012.
- 966 Warren, C. R.: Terminal environment, topographic control and fluctuations of West Greenland glaciers,
967 *20*, 1–15, <https://doi.org/10.1111/j.1502-3885.1991.tb00453.x>, 2008.
- 968 Yalcin, M.: The impact of topographical parameters to the glaciation and glacial retreat on Mount Ağrı
969 (Ararat), *Environ Earth Sci*, 78, 393, <https://doi.org/10.1007/s12665-019-8374-1>, 2019.
- 970 Yang, M., Wang, X., Pang, G., Wan, G., and Liu, Z.: The Tibetan Plateau cryosphere: Observations and
971 model simulations for current status and recent changes, *Earth-Science Reviews*, 190, 353–369,
972 <https://doi.org/10.1016/j.earscirev.2018.12.018>, 2019.
- 973
- 974
- 975
- 976
- 977
- 978
- 979
- 980
- 981
- 982
- 983
- 984
- 985
- 986
- 987
- 988
- 989
- 990



991 **Tables:**

Data type	Source	Resolution (m/time)	Acquisition time/period
Optical	Orthoimages IGN	0.2	July 2015
	Pleiades 1A PAN	0.5	25/08/2019, 19/08/2012
	Sentinel 2	10	12/09/2019
	SPOT 6	2.2	14/09/2019
	Pleiades 1A XS	2	19/08/2012
	Orthoimages IGN	0.5	July 2001
	Orthoimages IGN	0.5	1952
	SAFRAN reanalysis	daily	1958 - 2019
Meteorological	Col du Grand-Saint Bernard weather station (2469 m a.s.l.)	daily	1952 - 2019
	Aiguille du Midi weather station (3840 m a.s.l.)	daily	2007-2018

992

Table 1: Datasets used for the study.

993

Variable	Time-period	R²	Pearson's r
Direct Solar Radiation	1952 - 2001	0.64	0.79
	2001 - 2012	0.67	0.81
	2012 - 2019	0.51	0.72
Elevation	1952 – 2001	0.61	-0.78
	2001 - 2012	0.57	-0.75
	2012 - 2019	0.51	-0.71
	1952 - 2001	0.40	0.63
	2001 - 2012	0.34	0.58



MARST	2012 - 2019	0.27	0.52
TRI	1952 - 2001	0.37	0.60
	2001 - 2012	0.30	0.55
	2012 - 2019	0.32	0.57
Slope	1952 - 2001	0.29	0.54
	2001 - 2012	0.25	0.50
	2012 - 2019	0.21	0.46
Curvature	1952 - 2001	0.06	-0.26
	2001 - 2012	0.03	-0.18
	2012 - 2019	0.06	-0.24
Size of IA	1952 - 2001	0.04	-0.22
	2001 - 2012	0.06	-0.26
	2012 - 2019	0.04	-0.22

994 Table 2: Linear regression parameters and correlation metrics for each studied parameter.

995

996

Time pe- riod	Slope	Intercept	R²	Pearson's r	RMSE (km²)	p value
1952 - 2001	0.79	0.12	0.53	0.73	0.010	< 0.001
2001 - 2012	0.70	0.26	0.56	0.75	0.102	< 0.001
2012 - 2019	0.89	0.04	0.63	0.80	0.097	< 0.001

997

(a)

998

Time pe- riod	Slope	Intercept	R²	Pearson's r	RMSE (km²)	p value
1952 - 2001	1.01	-0.04	0.73	0.86	0.075	< 0.001
2001 - 2012	0.74	0.22	0.67	0.82	0.086	< 0.001



2012 - 2019	1.37	-0.39	0.83	0.91	0.071	< 0.001
--------------------	------	-------	------	------	-------	---------

999

(b)

1000 Table 3: Linear regression parameters and correlation metrics for each time-period (a) using
1001 AdM transformed data and (b) using the SAFRAN reanalysis product.

1002

1003

1004

1005

1006

1007

1008

1009

1010

1011

1012

1013

1014

1015

1016

1017

1018

1019

1020

1021

1022

1023

1024

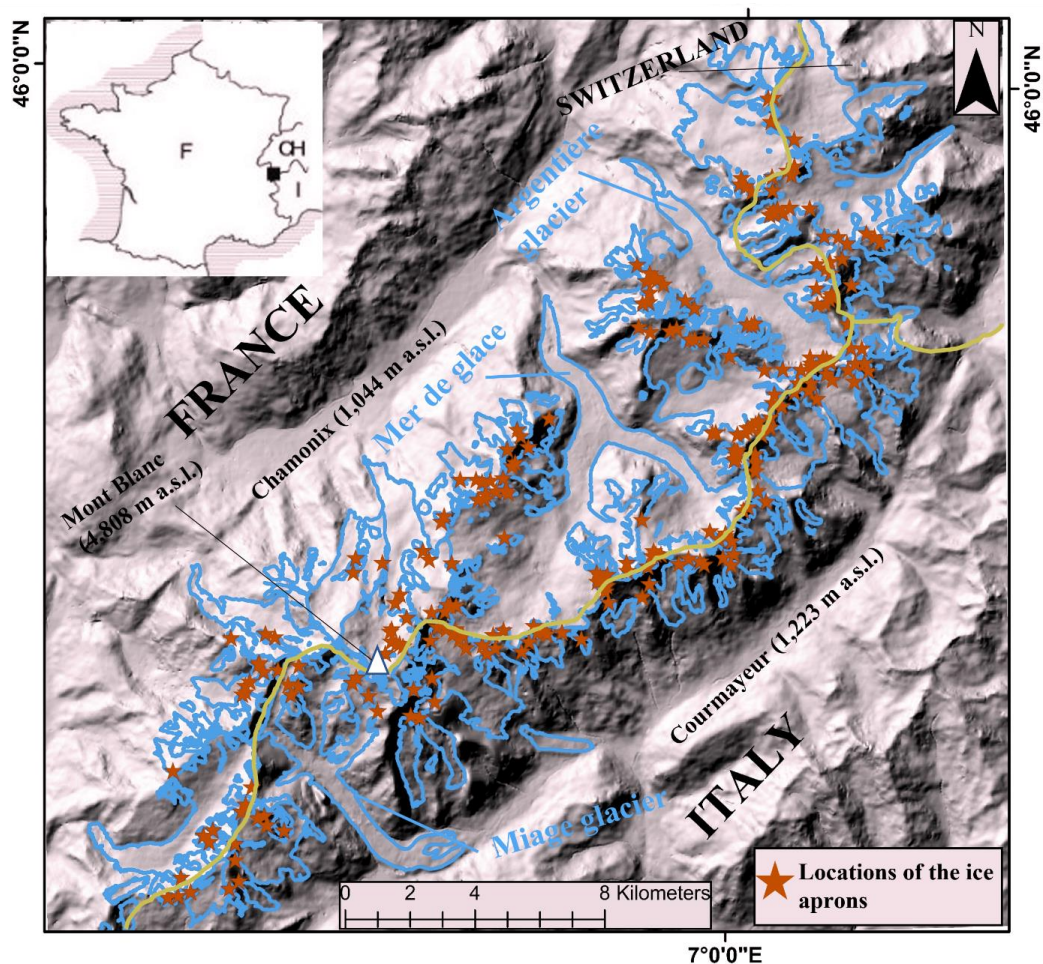
1025

1026

1027



1028 **Figures:**

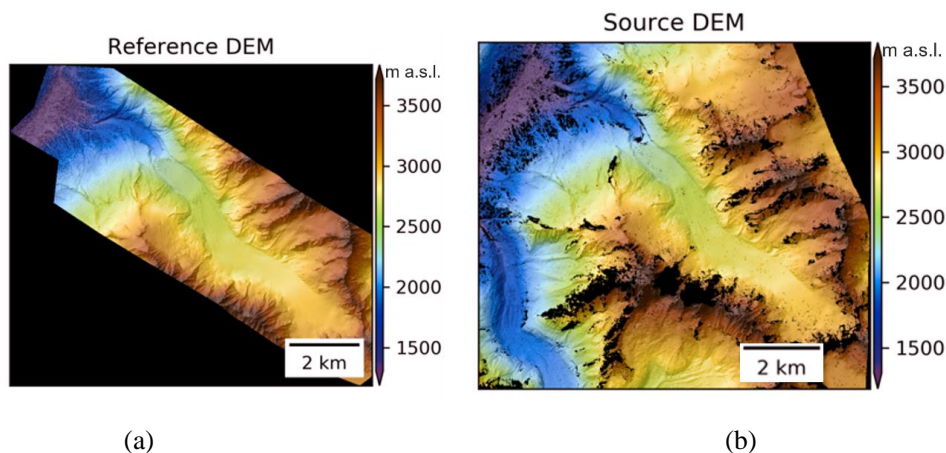


1029

1030 Figure 1: The Mont-Blanc massif (Western European Alps). 200 IAs (red stars) were digitized
1031 accurately on high-resolution images. The glacier outlines (in blue) comes from Gardent et al.,
1032 2014.

1033

1034

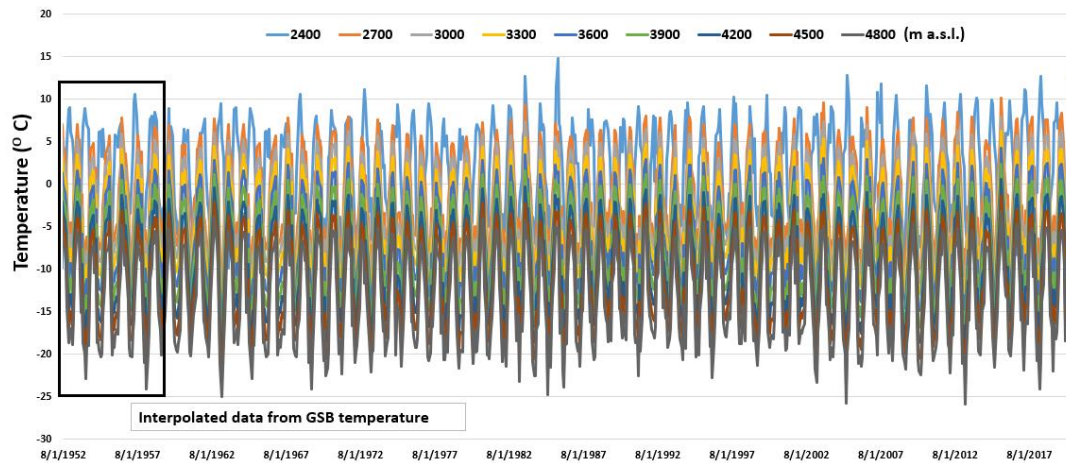


1035

1036

1037 Figure 2: (a) The reference LiDAR DEM of the Argentière glacier used for co-registration, (b)
1038 the source Pleiades DEM used for further analysis.

1039



1040

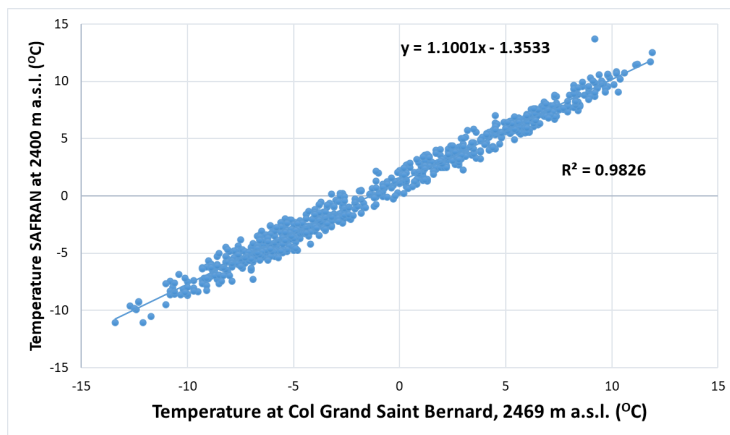
1041 Figure 3: SAFRAN reanalysis product temperature time-series from 1952-2019 for different
1042 elevations in the MBM. The figure shows mean August temperatures, the peak summer month in
1043 the Alps.

1044

1045

1046

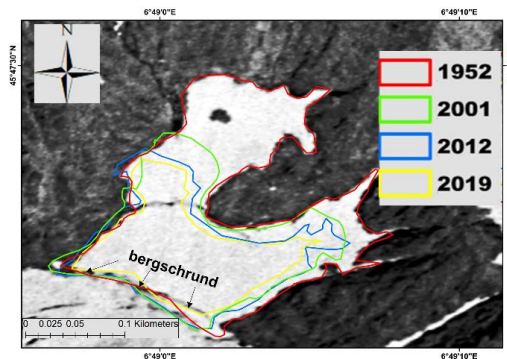
1047



1048

1049 Figure 4: Correlation between the monthly averaged temperature measurements at the Col du
1050 Grand Saint Bernard (GSB) and the SAFRAN reanalysis data at 2400 m a.s.l.

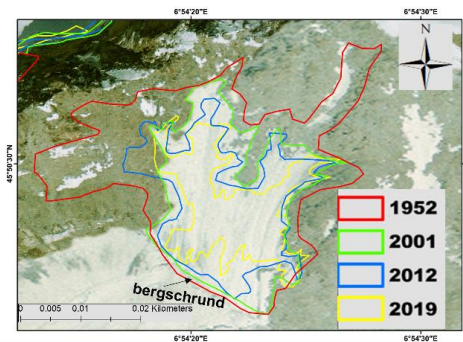
1051



1052

1053

(a)



1054

1055

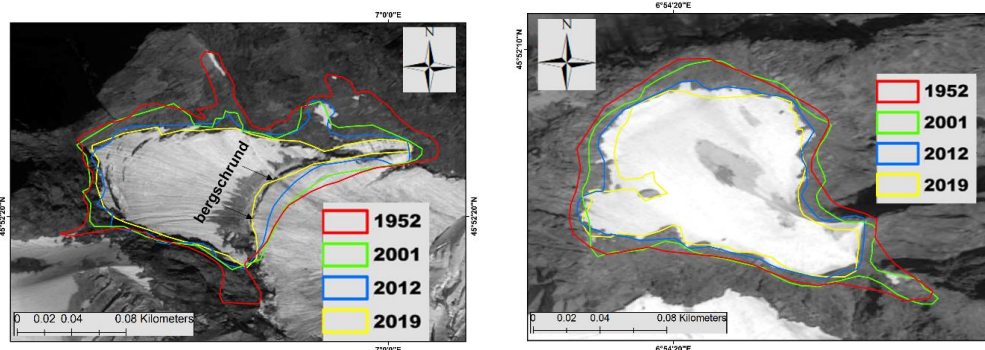
1056

1057

1058

1059

(b)



1060

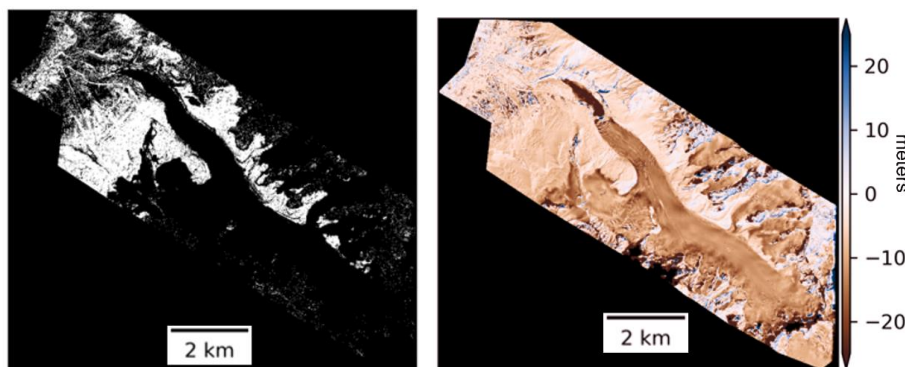
1061

(c)

(d)

1062 Figure 5: IAs extent delineated on high-resolution images: (a) orthophotos 1952, (b) orthophotos
1063 2001, (c) Pleiades panchromatic 2012, (d) Pleiades panchromatic 2019. The different colour
1064 polygons represent the surface area for each date.

1065



1066

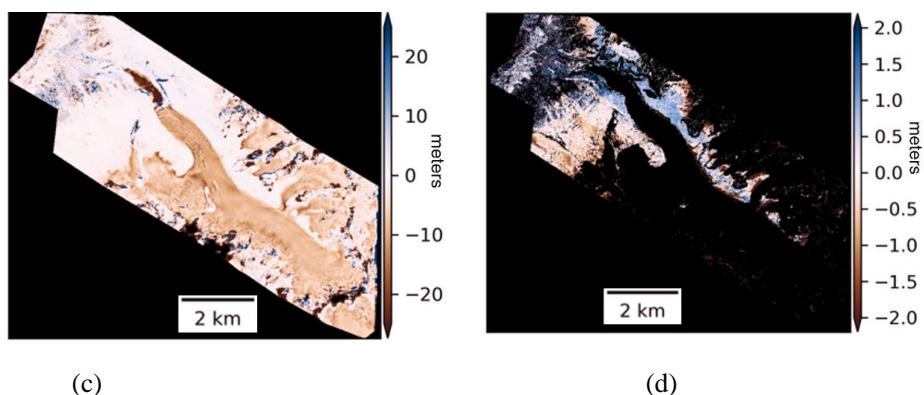
1067

(a)

(b)

1069

1070

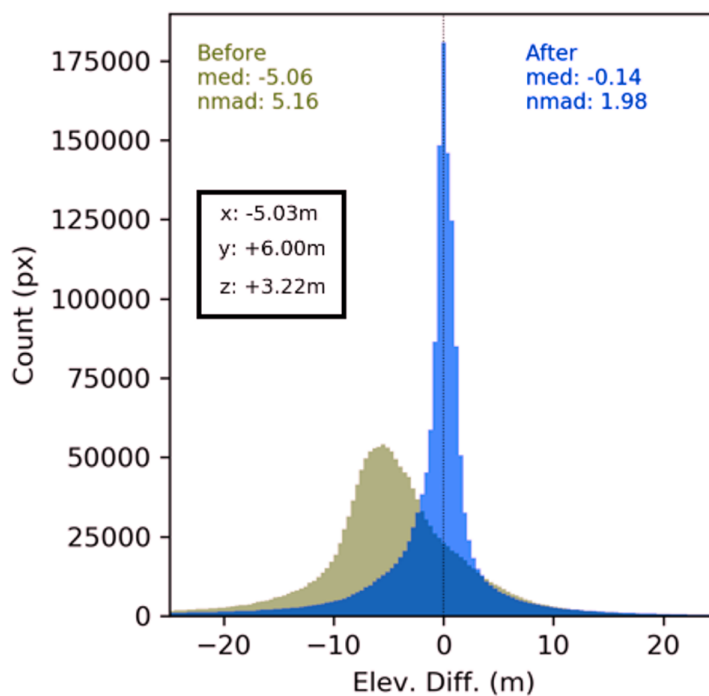


1071

1072

1073

1074 Figure 6: Stepwise Pleiades DEM accuracy assessment (a) the surfaces used for coregistration
1075 (b) elevation difference before coregistration (c) elevation difference after coregistration
1076 considering all areas (d) elevation difference after coregistration considering only the stable
1077 areas.



1078

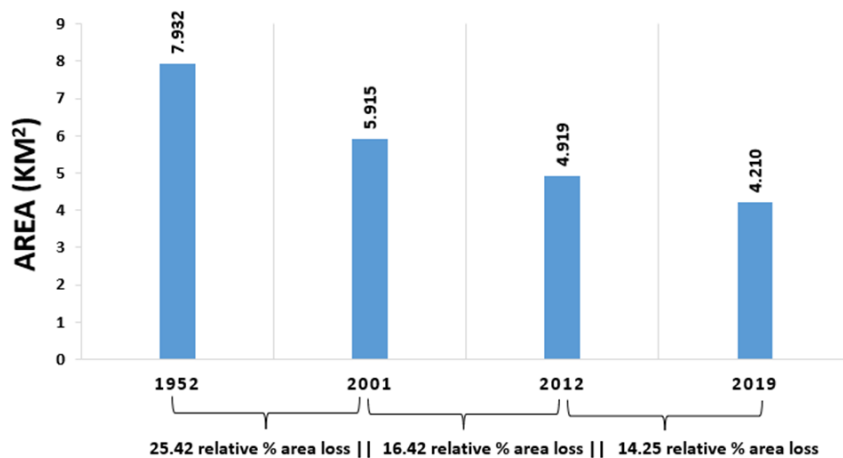
1079

1080 Figure 7: DEM Error (elevation difference between the reference and source DEM) distribution
1081 for stable areas



1082

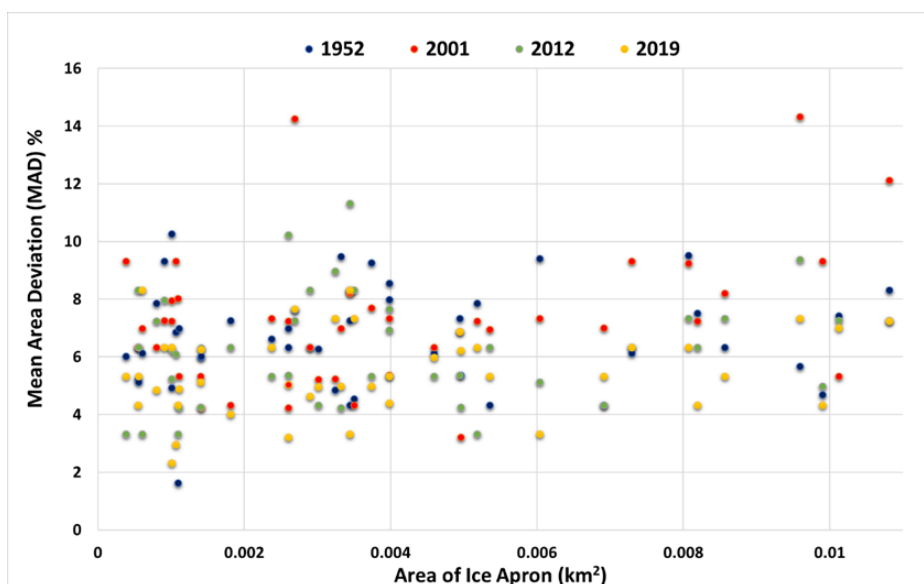
1083



1084

1085 Figure 8: A comparison of the total surface area of all IAs (423 IAs) in the MBM over 67 years.

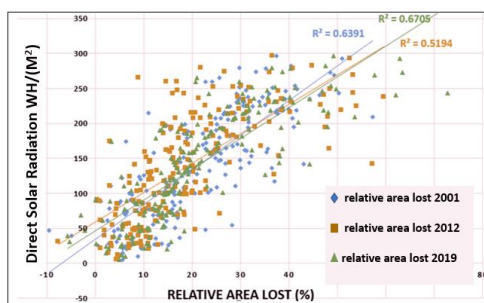
1086



1087

1088 Figure 9: The distribution of MAD values based on multiple digitizations of the IAs area for all
1089 periods.

1090



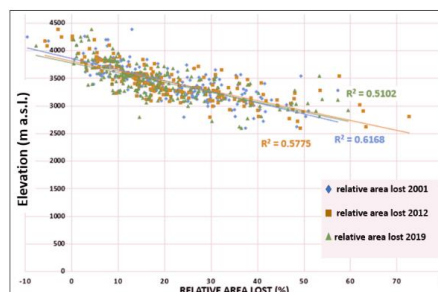
1091

1092

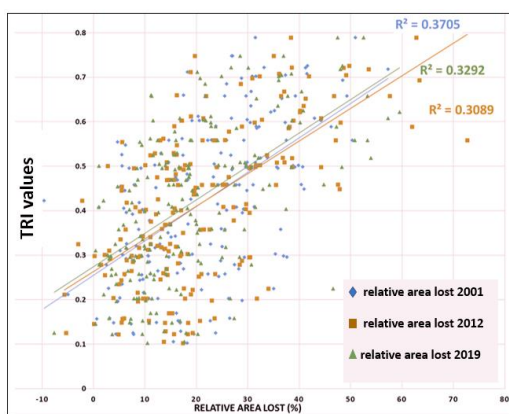
1093

1094

(a)



(b)

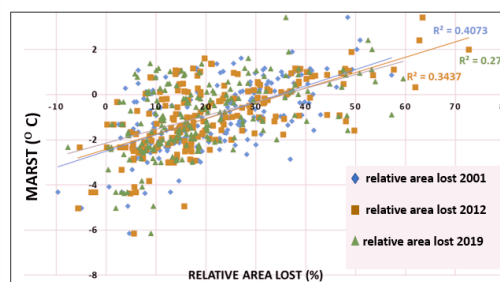


1095

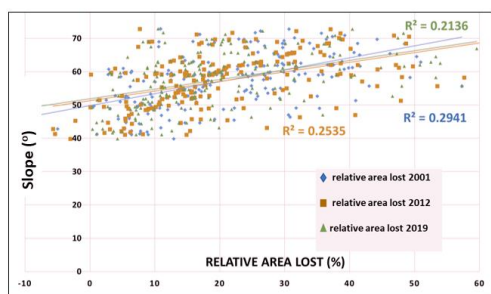
1096

1097

(c)



(d)

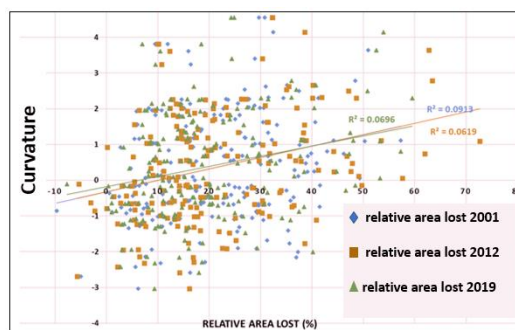


1098

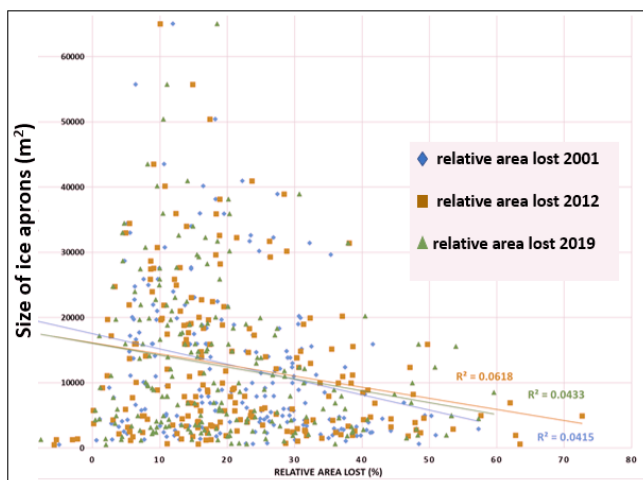
1099

1100

(e)



(f)



1101

1102

1103

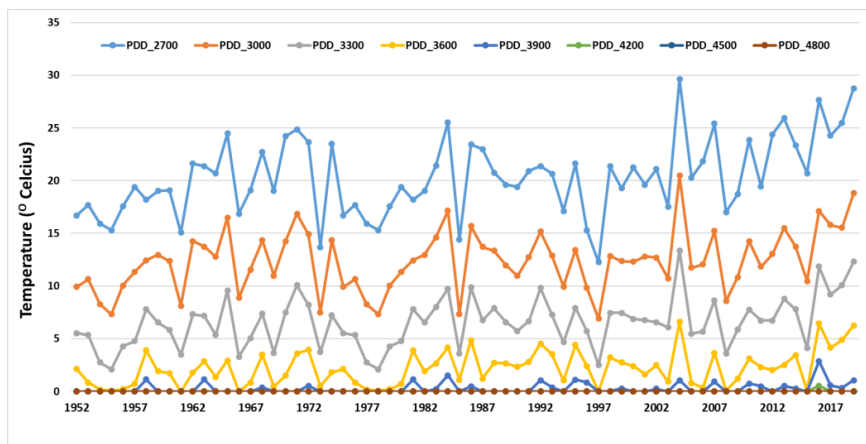
(g)

1104

1105 Figure 10: Scatter plots showing relationships between topographic factors and the area loss of
1106 IAs from 1952 to 2019. a) Direct solar radiation, b) elevation, c) TRI, d) MARST, e) slope, f)
1107 curvature and f) size of the IAs.

1108

1109



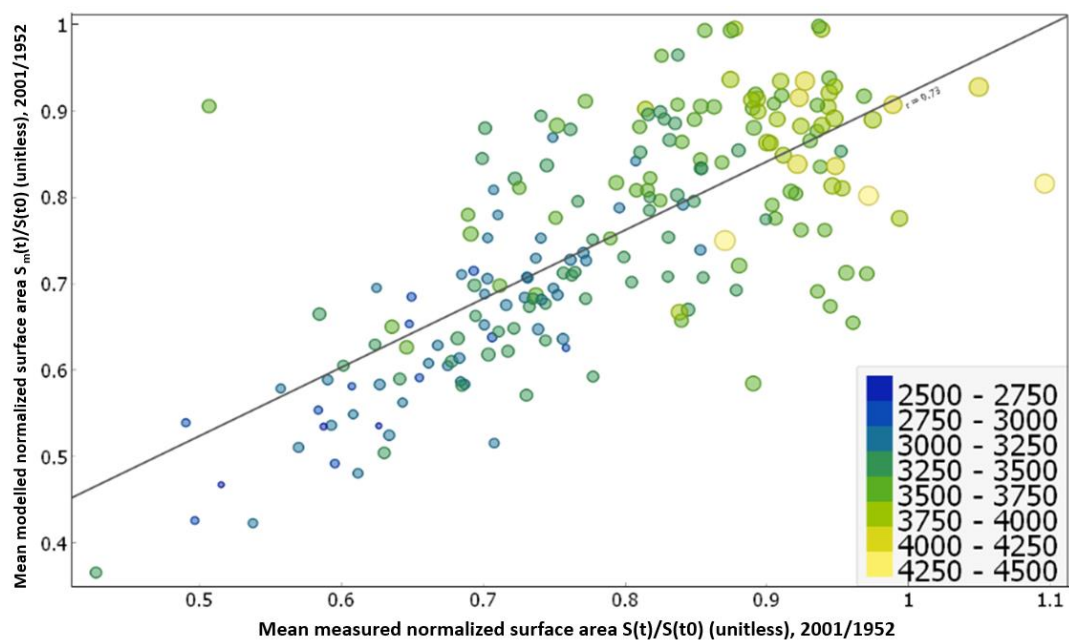
1110

1111

1112 Figure 11: The variation of annual PDD values at different elevations in the MBM from 1952 to
1113 2019.



1114

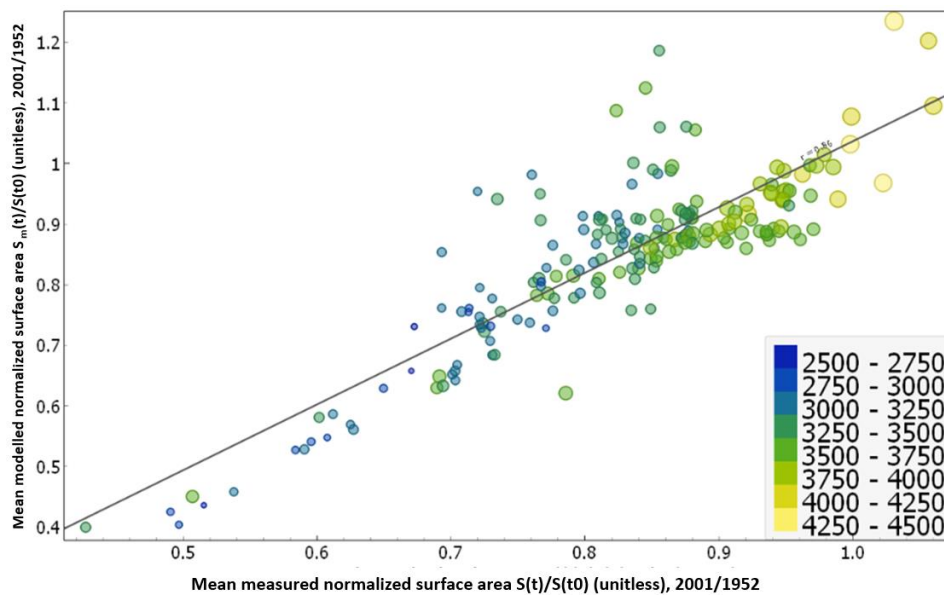


1115

1116

(a)

1117



1118

1119

(b)



1120

1121 Figure 12: Correlation between the mean normalized surface area estimates and the modelled
1122 surface areas. $S(t)/S(t_0)$ represents the normalization of the surface area measurement at time t by
1123 the initial value. Similarly, $S_m(t)/S(t_0)$ represents the normalization of the modelled surface area
1124 (a) with GSB data transformed to AdM data and (b) with SAFRAN reanalysis data at time t . The
1125 colour and size of the ticks represent the mean elevation of the IA.

1126

1127